The Thesis Committee for Brent Wise
Certifies that this is the approved version of the following thesis:

Addition of Platinum to Palladium-Cobalt Nanoalloy Catalyst by Direct Alloying and Galvanic Displacement

APPROVED BY
SUPERVISING COMMITTEE:

Supervisor:

Arumugam Manthiram

Paulo Ferreira

Addition of Platinum to Palladium-Cobalt Nanoalloy Catalyst by Direct Alloying and Galvanic Displacement

by

Brent Wise, B.S.

Thesis

Presented to the Faculty of the Graduate School of

The University of Texas at Austin

in Partial Fulfillment

of the Requirements

for the Degree of

Master of Science in Engineering

The University of Texas at Austin

December 2010

Acknowledgements

I would like to thank my advisor, Professor Arumugam Manthiram for allowing me to further my education as a member of his research group. I would also like to thank Professor Paulo Ferreira for being the reader for my thesis.

I am grateful to Dr. Xinsheng Zhou for showing me how to prepare membrane electrode assemblies and performing fuel cell tests on my samples. I am also thankful to Dr. Hao Liu for answering my questions about electrochemical testing and synthesizing nanoparticles.

December 2010

Abstract

Addition of Platinum to Palladium-Cobalt Nanoalloy Catalyst by Direct Alloying and Galvanic Displacement

Brent Wise, M.S.E.

The University of Texas at Austin, 2010

Supervisor: Arumugam Manthiram

Direct methanol fuel cells (DMFC) are being investigated as a portable energy conversion device for military and commercial applications. DMFCs offer the potential to efficiently extract electricity from a dense liquid fuel. However, improvements in materials properties and lowering the cost of the electrocatalysts used in a DMFC are necessary for commercialization of the technology. The cathode electrocatalyst is a critical issue in DMFC because the state-of-the-art catalyst, platinum, is very expensive and rare, and its performance is diminished by methanol that crosses over from the anode to the cathode through the Nafion membrane.

This thesis investigates the addition of platinum to a palladium-cobalt nanoalloy electrocatalyst supported on carbon black in order to improve catalyst activity for the

oxygen reduction reaction (ORR) and catalyst stability against dissolution in acidic environment without significantly reducing the methanol-tolerance of the catalyst. Platinum was added to the palladium-cobalt nanoalloy catalyst using two synthesis methods. In the first method, platinum was directly alloyed with palladium and cobalt using a polyol reduction method, followed by heat treatment in a reducing atmosphere to form catalysts with 11 and 22 atom % platinum. In the second method, platinum was added to a palladium-cobalt alloy by galvanic displacement reaction to form catalysts with 10 and 22 atom % platinum. The palladium cobalt alloy was synthesized using a polyol method, followed by heat treatment in a reducing atmosphere to alloy the nanoparticles before the Pt displacement. It was found that both methods significantly improve catalyst activity and stability, with the displaced catalysts showing a higher activity than the corresponding alloy catalyst. However the alloy catalysts showed similar resistance to dissolution as the displaced catalysts, and the alloyed catalysts were more tolerant to methanol. The displaced catalyst with 22 atom % platinum (8 wt. % Pt overall) performed similar to a 20 wt. % commercial platinum catalyst in both RDE and single cell DMFC tests. The 10 and 22 atom % Pt displaced catalysts and 22 atom % Pt alloyed all showed higher Pt mass specific activities than a commercial Pt catalyst.

Table of Contents

List of Tables

List of Figures

CHAPTER 1

INTRODUCTION

1.1 FUEL CELL FUNDAMENTALS

Fuel cells are devices that convert the energy released in the reaction of a fuel and an oxidant directly to electricity. Unlike heat engines, which extract work by first converting the chemical energy stored in the fuel and oxidant to heat, fuel cell efficiency is not limited by the Carnot cycle efficiency [1]. Typical efficiency of an internal combustion engine is 20-30%. Fuel cells are capable of efficiencies significantly higher than this; expected efficiency for a proton exchange membrane fuel cell operated on hydrogen is above 50% [2]. Therefore, replacing internal combustion engines with fuel cells could lead to large energy savings without a corresponding reduction in energy output. In addition to fuel efficiency, a fuel cell operating with hydrogen fuel has the added benefit of not producing greenhouse gases or other pollutants such as NO_x gases or particulates that an internal combustion engine requires catalysts and filters to contain.

A fuel cell is made up of three major parts: an anode, electrolyte, and cathode as shown in Figure 1.1. Fuel, typically hydrogen or a hydrocarbon, is fed to the anode where it is electro-oxidized to form cations and electrons. The electrons travel through an external circuit to the cathode where they are used to electro-reduce the oxidant. The electrolyte between the anode and cathode conducts ions, but not electrons. Fuel cells are characterized by the type of ion the electrolyte conducts. This will be discussed further below. Electrolytes must conduct either the cation product formed by the oxidation at the anode or the anion product formed by the reduction at the cathode. In an operating fuel cell, one type of ion travels through the electrolyte to the opposite electrode where the cation and anion react to form the final product, which is then removed from the fuel cell.

Fuel cells generate electricity in the form of the electron current through the external circuit connecting the anode and cathode. Energy can be removed from this current because there is an electrochemical potential difference between the anode and cathode due to the reactions occurring at each.

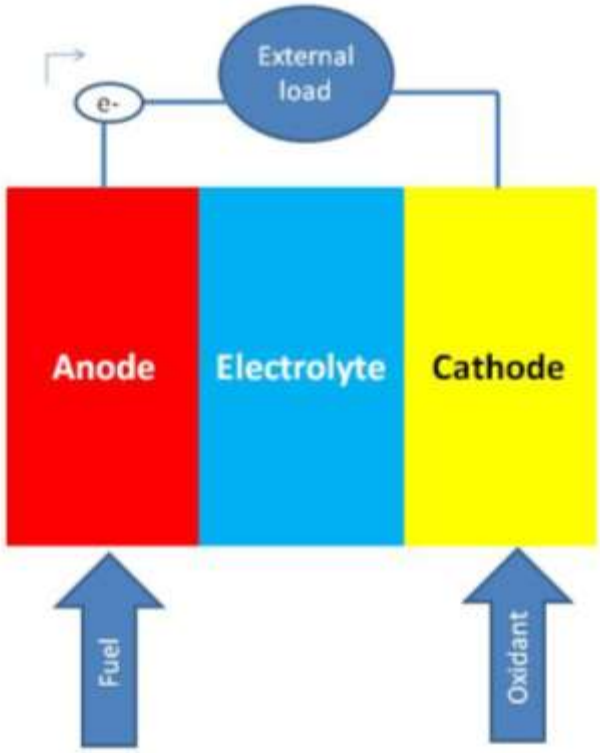

Figure 1.1 Simple representation of a fuel cell. Fuel is oxidized at the anode.

Fuel cells are classified by the electrolyte used. There are four electrolytes being considered, and each has different operating requirements including fuel and temperature range. These include acid (protons), alkaline (hydroxide ions), carbonate ions, and oxide ions. Acid fuel cells conduct protons (H^+) through the electrolyte from the anode to the cathode. Alkaline fuel cells conduct hydroxide ions (OH^-) through the electrolyte from the cathode to the anode. Molten carbonate fuel cells conduct carbonate anions (CO_3^{2-}) through the electrolyte from cathode to anode. Finally, solid oxide fuel cells conduct

oxide ions (O^{2-}) through the electrolyte from the cathode to the anode. Table 1.1 outlines the typical operating conditions of different types of fuel cells.

Acid fuel cells can be further classified by the type of acid that constitutes the electrolyte. Polymer electrolyte membrane fuel cells (PEMFC) use a solid acidic polymer film, such as Nafion as the electrolyte, phosphoric acid fuel cells use hot liquid phosphoric acid, and solid acid fuel cells use a proton-conducting ceramic membrane. A PEMFC fueled directly with an aqueous solution of methanol is referred to as a direct methanol fuel cell (DMFC). The DMFC is the subject of this thesis and it will be explained in more detail in the section below.

Table 1.1 Different types of fuel cells with typical operating conditions.

Fuel cell type	Electrolyte Material	Operating temperature	Fuel
Solid oxide	Yttria stabilized zirconia	600 ºC – 800 ºC	H_2, CH_4
Molten carbonate [3]	Molten Na_2CO_3	600 ºC – 700 ºC	CH_4, C_3H_8
Alkaline [4]	Aqueous KOH	RT – 100 ºC	H_2
Phosphoric Acid	Liquid H_3PO_4	150 °C – 200 °C	H_2
Polymer electrolyte membrane	Nafion	RT – 100 ºC	H_2
Direct methanol	Nafion	RT – 100 ºC	CH_3OH
Solid acid [5]	CsH_2PO_4	100 ºC – 300 ºC	H_2

1.2 DIRECT METHANOL FUEL CELL PRINCIPLES

DMFCs use a proton conducting membrane as electrolyte, and an aqueous methanol solution is used as the fuel. Methanol is electro-oxidized by a catalyst at the anode according to the methanol oxidation reaction (MOR) [6]:

$$CH_3OH + H_2O \rightarrow CO_2 + 6H^+ + 6e^- \quad (1.1)$$

The standard electrochemical potential (E^o) for this reaction is $E^o = 0.039$ V vs normal hydrogen electrode (NHE) [6]. Oxygen is fed to the cathode where it combines with the protons and electrons generated in the anode reaction to form water by the oxygen reduction reaction (ORR):

$$3/2\ O_2 + 6H^+ + 6e^- \rightarrow 3H_2O \quad (1.2)$$

The standard electrochemical potential for the ORR is $E^o = 1.229$ V vs. NHE [7]. Based on equations (1.1) and (1.2), the overall DMFC reaction is:

$$CH_3OH + 3/2\ O_2 \rightarrow CO_2 + 3H_2O \quad (1.3)$$

The overall maximum cell potential (ΔE^o) for the reaction is 1.19V vs. NHE.

In usage, this cell potential cannot be attained. There are polarization losses associated with the kinetics of electrode reactions, mass transfer limitations, and resistance to current flow [7-9].

Polarization contributed by resistance to current flow is termed ohmic loss, since the cell behaves essentially like a resistor in an electric circuit. The potential drop is proportional to the current through the material [10]. Ohmic loss contributions arise from anywhere in the cell that resists current including the electronic resistance in the electrodes and ionic resistance in the electrolyte. The electrolyte is a proton conductor with a finite resistance to conduction similar to electrical resistors in circuits. Like electrical resistors, electrolyte resistance is roughly proportional to the proton current

flowing through it. Therefore, the ohmic polarization (η_{Ω}) can be estimated by the following equation [10]:

$$\eta_{\Omega} = iR \qquad (1.4)$$

where i is the current passing through the cell, and R is the overall resistance of the fuel cell including ionic and electronic terms. Because of the one-to-one correspondence of protons and electrons in equation (1.1), the electronic current through the external circuit is equal to the ionic current through the electrolyte.

There are overpotential contributions arising from processes at both electrodes. The first is activation overpotential due to the MOR at the anode ($\eta_{Act,a}$), and the second is activation overpotential due to the ORR at the cathode ($\eta_{Act,c}$). Collectively this overpotential is labeled (η_{Act}). The MOR and ORR reactions both suffer from sluggish kinetics, so significant driving forces are necessary for the reactions to proceed at a significant rate [11]. In a PEM fuel cell, the hydrogen oxidation reaction at the anode is very rapid so that almost all of the activation polarization is due to the reaction at the cathode [10]. In a DMFC, activation overpotentials at the anode and cathode are significant. It is difficult to separately measure the activation polarization from the cathode and from the anode in an operating DMFC since polarization curves show only the measured potential at a given current.

Concentration polarization (η_{Conc}) occurs when the reactants at both the anode and cathode are consumed as rapidly as they can be transported to the catalyst surface [7]. Increasing the overpotential (decreasing the potential difference between anode and cathode) does not increase the current because the concentration of reactants (methanol or oxygen) at the electrode surface is zero. Mass transfer to the electrodes would have to be improved to increase the current.

The overall cell potential of an operating DMFC (E_{cell}) is given by the standard cell potential minus the sum of the individual polarization losses [10].

$$E_{cell} = \Delta E^{o} - (iR_E + \eta_{Act,a} + \eta_{Act,c} + \eta_{Conc}) \quad (1.5)$$

Figure 1.2 shows a typical polarization curve for a DMFC. The dominant contributor to the potential loss in each region is labeled. At small currents, the activation overpotential dominates. The ohmic loss is negligible since it is proportional to the current. The concentration overpotential is also negligible since the reaction rates at both the anode and cathode are low and reactant concentration gradients are small. The overall activation overpotential ($\eta_{Act,a} + \eta_{Act,c}$) in the low current region is about 0.6 V as shown in the figure. The activation overpotential is about half of E_{cell}. Therefore, the overall cell efficiency is limited to 50%. As more current is drawn in the cell, the potential drop across the electrolyte becomes more significant, while the activation overpotentials do not increase significantly. The iR_E term dominates the cell losses in this region. As the current increases further, the concentrations of reactants at the electrodes are driven to zero and mass transfer rates limit the current.

From the discussion above and the plot in Figure 1.2 it is obvious that the activation overpotentials at both the anode and cathode greatly limit the overall efficiency of a DMFC. Since both the MOR and ORR follow catalytic pathways, discovering new catalysts for each reaction with improved kinetics is critical for developing and commercializing the DMFC technology.

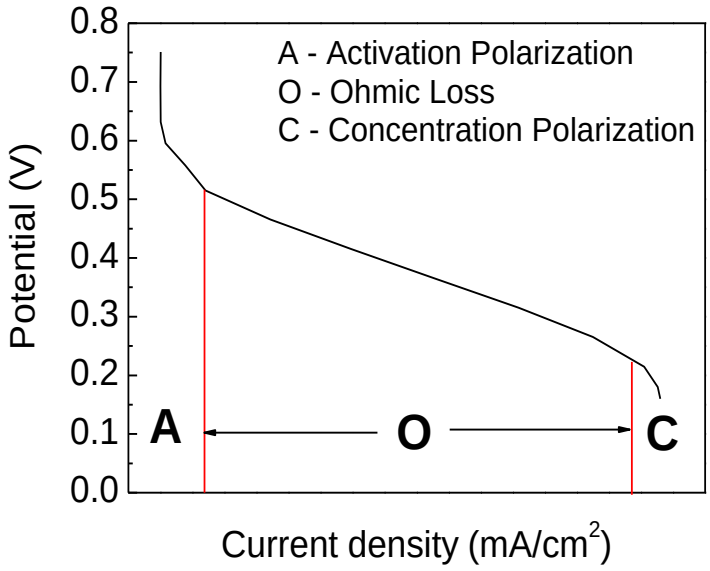

Figure 1.2 A typical polarization curve for a direct methanol fuel cell, showing the regions where activation, ohmic, and concentration polarization losses dominate.

1.3 STATE-OF-THE-ART DMFC MATERIALS

The state-of-the-art DMFC consists of a platinum-ruthenium nanoparticle catalyst for the anode, a platinum nanoparticle cathode catalyst, and a Nafion polymer membrane electrolyte [12].

The anode catalyst contains a mixture of the two rare precious metals, platinum and ruthenium. The MOR mechanism is not completely understood and will not be discussed in detail. Adsorbed carbon monoxide (CO) forms as an intermediate during the reaction. CO is difficult to oxidize on platinum at low temperature without further increasing the potential [13]. Ruthenium is added to the catalyst because it assists in CO oxidation [1]. Ruthenium is not stable in the anode, so it dissolves over time and the

anode reaction rate drops as CO forms on the platinum catalyst blocking reaction sites. In addition, while PtRu is the most active catalyst for the MOR, it still suffers from a large activation overpotential [15]. Other catalysts that have been investigated to overcome the poisoning effect of CO include platinum alloys such as platinum-tin [16], platinum-molybdenum [17] and platinum-lead [18]. The inclusion of nanostructured supports with platinum have also been considered including titanium dioxide [19], titanium nitride [20], and cerium oxide [21, 22]. Very few non-platinum containing catalysts have been considered because activation overpotentials are much larger.

Nafion is the state-of-the-art membrane electrolyte for DMFCs because it has high proton conductivity and it is very durable [23]. Nafion is a fluorinated polymer containing a backbone similar to polytetrafluorethane with fluorinated side chains containing sulfonic acid groups. The sulfonic acid groups form channels in the membrane giving protons a path to conduct via a vehicle mechanism [24]. In the vehicle mechanism, protons attached to water molecules (H_3O^+) can interact with the hydrophilic sulfonic acid groups and move from the anode to the cathode with little resistance. Unfortunately, these channels also attract methanol from the anode leading to two problems. The methanol-water mixture causes the membrane to swell, and methanol diffuses through the membrane to the cathode [25]. Membrane swelling increases the resistance of the cell. Methanol cross-over decreases fuel utilization since any methanol that reaches the cathode cannot be electro-oxidized at the anode. It exits the fuel cell with water generated at the cathode or it is oxidized on the cathode. Methanol cross-over can also hinder the ORR at the cathode, especially on good methanol oxidation catalysts such as platinum [26]. To solve the methanol cross-over problem, the Nafion membrane can be made thicker to decrease the methanol flux, but this leads to a larger cell resistance because membrane resistance is proportional to the distance protons must travel though it [25].

Inert material can be added to the membrane to block methanol diffusion, but this also increases the resistance [27].

Other membrane materials have been investigated to replace Nafion because Nafion is expensive to produce and is permeable to methanol. These include sulfonated poly ether ether ketone (SPEEK), and polybenzimidazole [28, 29]. SPEEK membrane is much cheaper to synthesize than Nafion since it contains no fluorine. SPEEK can be made with proton conductivity close to Nafion, but it suffers from similar methanol cross-over problems [30]. SPEEK membranes can be blended with polymers containing basic heterocycles to decrease methanol cross-over without also decreasing proton conductivity [31, 32].

DMFC cathodes are the focus of this thesis and will be discussed in greater detail than the anode or electrolyte in a separate section below.

1.4 DMFC CATHODES

1.4.1 The Oxygen Reduction Reaction in Acid

The reaction that occurs at the DMFC cathode is the ORR, the same reaction that occurs in the hydrogen fueled PEMFC, equation (1.2). This is one of the most studied reactions in chemistry because of its importance in energy conversion devices and biological reactions [33 – 35]. The ORR has an equilibrium potential of 1.229 V vs. NHE, but in practice a potential above 1.0 V is never attained on even the most active catalysts [33]. This large activation overpotential limits the energy efficiency to less than 80 % without considering any other losses in the system.

From equation (1.2), four electrons are transferred from the cathode for each molecule of oxygen consumed. Since four electrons are involved, the mechanism is

necessarily complex [7]. The mechanism for the ORR on platinum, the most studied catalyst, is still open to debate. The most widely-accepted mechanism was first proposed by Wroblowa, Pan, and Razumney in 1976 [36, 37]. It is shown schematically in Figure 1.3. In this mechanism, O_2 diffuses to the catalyst surface where it is absorbed non-dissociatively. In a series of four electron transfers (k_1), it can directly form water. It can reversibly form adsorbed hydrogen peroxide (k_2) in a series of two electron transfers. The adsorbed hydrogen peroxide can decompose to adsorbed oxygen (k_4), desorb (k_5) or form water in a second series of two electron transfers. The direct pathway is often referred to as the four electron pathway because four electron transfers occur in a rapid series. The reaction to form hydrogen peroxide is often referred to as the two electron pathway because two electrons are required to reduce one molecule of oxygen to hydrogen peroxide, and a further two electrons are needed to reduce hydrogen peroxide to two water molecules [7].

$$O_2 + 2e^- + 2H^+ \rightarrow HOOH \qquad (1.6)$$

$$HOOH + 2H^+ \; 2e^- \rightarrow 2H_2O \qquad (1.7)$$

The four electron pathway is more efficient, but both pathways can occur on different surfaces at the same time [37]. The two electron pathway is not desirable because it is less efficient. The standard electrochemical potential of equation (1.6) is only 0.695 V vs. NHE and it forms a strong oxidizing agent, hydrogen peroxide, which can deteriorate the membrane and other fuel cell components [38].

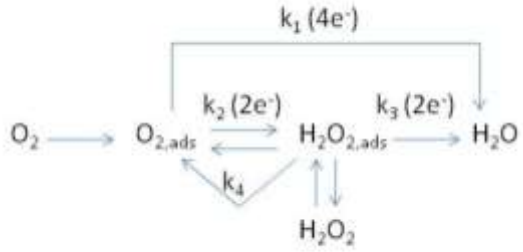

Figure 1.3 Schematic representation of the possible ORR paths on metal surfaces.

The reaction path and kinetics are surface dependent [37]. Different surface planes and defects have different surface energies. For large platinum single crystals, the (1 1 0) surface was found to have the most facile kinetics for the ORR reaction in $HClO_4$ electrolyte compared to the other low energy surfaces, (1 0 0) and (1 1 1) [39]. Surface defects such as vacancies and steps also influence reaction rates. For platinum, the smooth terrace surfaces show more facile ORR kinetics than step edges and kinks [40].

1.4.2 Material Properties Requirements for ORR Catalysts

ORR catalysts must efficiently reduce oxygen to water following the four electron pathway [1]. The larger the activation potential for the ORR, the less efficient the fuel cell, since the potential difference between anode and cathode is directly proportional to power density. The catalyst must adsorb oxygen to promote the electron transfer, but it must not adsorb oxygen so strongly as to trap oxygen on the surface and block the active reaction sites [37].

In addition to high activity for the ORR reaction, potential catalysts must be electrically conducting. The electrons removed from methanol in the anode need to travel as a current through the anode and cathode, so any resistance to electron conduction in either electrode is manifest as ohmic loss, which effects overall efficiency. The materials

must also be able to withstand an extreme environment. The pH in a DMFC is acidic since the membrane contains -SO_3H groups, the atmosphere contains oxygen, and the potential at the cathode is oxidizing. Since these conditions are very strongly oxidizing, typical engineering materials such as steel cannot survive long. For practical usage, the DMFC needs to operate for thousands of hours without a large decrease in performance, so material degradation is a critical issue.

The state-of-the-art catalyst for the ORR reaction in PEMFC and DMFC is platinum nanoparticles of 3 nm in size dispersed on carbon black. The size of the nanoparticles is crucial because the inherent activity increases with particle size [40], but the number of active sites per mass of platinum increases as the particle size decreases. Due to the trade-off, 3 nm particles have been shown to have the best ORR performance [41]. Decreasing the particle size below 3 nm also destabilizes the nanoparticles against dissolution [41].

For DMFCs, the additional complication of methanol cross-over further limits the potential ORR catalysts to those tolerant to methanol. The-state-of-the-art ORR catalyst, platinum nanoparticles supported on carbon black is also a great oxidation catalyst [42]. At DMFC operating temperatures, any methanol that reaches the cathode is easily oxidized in the oxygen rich atmosphere.

1.4.3 Alternative ORR catalysts for DMFC

Platinum is very expensive and rare. While it is the current state-of-the-art catalyst, it is not viable for many commercial applications because of its high cost [43]. Therefore, much effort has been put forth to discover catalysts that either contain less or no platinum. The highlights of this field will be briefly summarized in this section.

When platinum is alloyed with some transition metals, its activity for the ORR reaction significantly increases. Elements such as Cr [44], V [45], Fe [46], Ni [47] and Co [48] enhance performance when they are alloyed with Pt. The reason for the higher activity is attributed to changes in the d-band electron configuration of Pt atoms upon alloying and contraction of the Pt-Pt inter-atomic distance [49]. All of the 3d transition metals cited above have atomic radii much smaller than platinum. Alloying platinum with these elements, therefore, reduces the Pt-Pt inter-atomic distance. Decreasing the inter-atomic distance between platinum atoms helps to cleave the bond between oxygen atoms in an adsorbed oxygen molecule on the metal surface [37]. Pt_3Co is one of the most studied platinum alloy catalysts. It shows kinetic currents per surface site about twice as large as platinum [48]. One limitation of platinum alloys is that the amount of bulk platinum atoms is not significantly reduced compared to platinum if the ratio of platinum to other metal is 3 : 1. Also, the transition metals are still unstable in acidic conditions, so they will dissolve over time [50]. It is difficult to make alloy nanoparticles of small size, because a heat treatment step at elevated temperature is typically required. This heat treatment causes the nanoparticles to grow in size, reducing the electrochemical surface area. It is difficult to make small nanoparticles if a heat treatment step is required for inter-atomic diffusion to alloy the nanoparticles.

A more active catalyst recently discovered is a dealloyed platinum-copper catalyst [51]. This catalyst has shown a platinum specific current density 4 times higher than platinum on a platinum weight basis. In this catalyst, copper-rich platinum-copper bimetallic nanoparticles are synthesized and then the copper is leached out by electrochemically cycling the potential. It is believed that the improved performance of this catalyst is due to the platinum enriched surface roughened shell of the alloyed nanoparticle, following copper dissolution [51].

Platinum-monolayer catalysts also show much higher activity than platinum catalysts [52, 53]. Platinum monolayer catalysts have a monolayer of platinum over a nanoparticle base. In theory, all of the platinum atoms can be active sites for the ORR since they are all on the surface of the catalyst. Platinum monolayers on palladium-transition metal alloy nanoparticles have performed very well and the complete layer of platinum on the surface prevents the nanoparticle base from dissolving under fuel cell operating conditions. Platinum monolayer catalysts are prepared by electrochemical underpotential deposition of a copper monolayer on the base nanoparticle surface followed by galvanically displacing the copper with platinum ions. This underpotential deposition method only works on noble nanoparticles such as rhodium or palladium [66], and it is difficult to scale-up to prepare large quantities of catalyst.

In addition to platinum monolayer catalysts, other platinum-rich shell core-shell catalysts have been studied. A few monolayers of mixed platinum and iron deposited on palladium or gold nanoparticles followed by removal of the iron also generates a highly active ORR catalyst [54, 55]. Sub-monolayer Pt catalysts have been studied also [56]. All of the core-shell catalysts benefit from the reduced amount of platinum required. All of the platinum atoms are located at or near the surface instead of being buried in the bulk. These catalysts display higher ORR activity per mass of Pt than commercial platinum catalyst. Complete platinum monolayers also allow alloys and compounds to be used as the nanoparticle base because the platinum atoms on the surface form a barrier to dissolution [53].

Platinum-free catalysts have also been studied, but they show lower performance than platinum containing catalysts. Palladium is atomically similar to platinum, and it is much more abundant and cheaper than platinum. It shows ORR activity that increases dramatically when it is alloyed with transition metal elements such as cobalt [57].

Catalyst activity increases when palladium is alloyed with transition metals similar to platinum. This is caused by strain and electronic effects from the smaller more electropositive transition metals on the palladium atoms that weaken oxygen adsorption on palladium atoms [58]. Palladium has been alloyed with 3d transition metals such as Fe [59], Ni [60], Cu [61], and other elements including Mo [62], and W [63]. The alloying effects on ORR activity are stronger in palladium alloys than in platinum alloys as the shift in onset potential is more dramatic. The activity of PdFe is reported to be higher than commercial platinum catalyst [59]. Palladium alloys are very tolerant to methanol cross-over from the anode of a DMFC, but they are not stable at fuel cell operating conditions [64].

Transition metal macrocyclic compounds have also been investigated as ORR catalysts. These materials are made of heterocyclic organic compounds such as porphyrins that complex with transition metal ions including as iron and cobalt [65]. Progress in this area has been made recently and activities near that of Pt have been reported for an iron-heterocycle complex catalyst [66], but further progress is needed before this technology becomes viable. The active site in these catalysts is believed to be the metal cation or the nitrogen atoms in the heterocycles [66]. While these catalysts are much cheaper to produce than platinum they lack stability and many follow a predominantly two-electron ORR pathway.

Transition metal chalcogenides have been investigated in the past as ORR catalysts [67]. These catalysts typically contain a platinum-group metal such as ruthenium or iridium forming a compound with a chalcogenide such as selenium. Transition metal chalcogenides are very tolerant of methanol, but they are not as efficient as platinum catalysts. They produce a significantly large amount of hydrogen peroxide [68].

Some transition metal carbides and nitrides also show activity for the ORR. Molybdenum nitride [69], tungsten nitride [70], and titanium nitride [71] all show activity for the ORR. Tungsten carbide shows little activity for ORR, but when it is used in conjunction with platinum nanoparticles the resulting catalyst has higher ORR activity than a platinum catalyst [72]. Nitrides and carbides may be unstable under the oxidizing conditions of a fuel cell cathode, and their performance is much lower than platinum containing catalysts.

Many different cathode materials have been investigated, but only a few show promise for replacing the state-of-the-art platinum nanoparticle catalyst. All of these catalysts contain platinum in varying amounts. Because of the strong oxidizing conditions at the cathode in a DMFC, a noble metal such as platinum or gold is necessary if the active site for ORR is metallic.

1.5 OBJECTIVE

The objective of this thesis was to prepare ORR catalysts based on a palladium-cobalt nanoalloy by addition of small amounts of platinum using two different methods, alloying and galvanic displacement, to understand how the location of the platinum atoms in the catalyst affect its ORR activity and tolerance to methanol. The synthesis technique and performance of the palladium-cobalt alloy catalyst have been previously characterized. The catalyst is tolerant of methanol, but its activity is lower than a commercial platinum catalyst and its stability is not adequate for fuel cell applications. In the alloying method, platinum atoms were directly added to the nanoparticle synthesis procedure to form a tertiary alloy with platinum throughout the bulk of the nanoparticles. In the galvanic displacement method, platinum was added to the surface of the already

alloyed palladium-cobalt catalyst by galvanic displacement method. The prepared catalysts were then characterized using basic materials and electrochemical characterization techniques: X-ray diffraction, energy-dispersive spectroscopy, transmission electron microscopy, X-ray photoelectron spectroscopy, cyclic voltammetry, rotating disk electrode experiments, and single-cell DMFC tests.

CHAPTER 2

EXPERIMENTAL PROCEDURES

2.1 MATERIALS SYNTHESIS

Materials were synthesized starting with a polyol method described in greater detail in Chapter 3. Ethylene glycol acted as both the solvent and reducing agent for the formation of nanoparticles supported on carbon black. Following separation from solvent, the catalysts were heat treated in a reducing atmosphere in a tube furnace to alloy the nanoparticles. In the case of the galvanically displaced samples, the alloyed palladium-cobalt nanoparticles were suspended in a dilute solution of potassium chloroplatinate (II) and heated to 100 ºC for 90 minutes before being filtered and washed.

2.2 MATERIALS CHARACTERIZATION TECHNIQUES

2.2.1 ENERGY DISPERSIVE SPECTROSCOPY

Energy dispersive spectroscopy (EDS) is a semi-quantitative technique used to measure the elemental composition of a sample. The sample is bombarded with energetic electrons (20keV) from a source such as a scanning electron microscope. Core electrons are removed from the atoms in the sample. Electrons of higher energy inside the atom move to the vacated lower-energy state. In the process, energy is given off in the form of X-rays of distinct wavelengths for each element. The EDS analyzer counts X-rays as a function of wavelength, and can quantify the composition of the sample based on the likelihood of X-ray emission for different elements. EDS cannot identify hydrogen, helium or lithium due to their electron energy configurations. EDS is neither surface specific or surface sensitive since the high energy electrons penetrate far into the bulk of the sample. A JEOL JSM-5610 scanning electron microscope with Oxford Instruments

EDS attachment was used to determine the bulk composition of the catalysts for this study.

2.2.2 POWDER X-RAY DIFFRACTION

Powder X-ray diffraction (XRD) is a technique used to determine phases present in a material and the lattice parameters associated with those phases. XRD is based on the Bragg Law:

$$n\lambda = 2d \sin\theta \qquad (2.1)$$

where n is an integral number of wavelengths, (typically, n = 1), λ is the wave-length of incident X-ray radiation, d is the spacing between lattice planes and θ is the angle between the lattice plane normal and the incident X-ray beam. In XRD, a flat sample is subjected to an X-ray beam. The angle of the X-ray beam is rotated through an angle and diffracted X-rays are counted at each angle. The count is then plotted vs. 2θ, and the phases present and lattice parameters are calculated from the peaks in the plot.

All samples were characterized by XRD with Cu Kα radiation X-ray source. Patterns were fit with mixed Gaussian and Lorentzian profiles (80 % Gaussian) using Jade MDI software to calculate lattice parameters and estimate particle size.

2.2.3 X-RAY PHOTOELECTRON SPECTROSCOPY

X-ray photoelectron spectroscopy (XPS) was used to determine near surface composition of samples. In XPS, the samples are irradiated with monochromatic X-rays. These X-rays remove core electrons from the sample. The XPS analyzer detects the kinetic energy of emitted electrons, from which the binding energy of the emitted electrons can be determined. Binding energies are specific to elements and vary with oxidation state. Binding energy increases with increasing oxidation state. Therefore elements present and oxidation state can be measured using XPS. The method is surface

sensitive because the emitted electrons have a very short mean free path before they are scattered inelastically by other atoms in the sample. Thus only a few nanometers of material near the surface can be analyzed.

For this thesis a Kratos Analytical spectrometer with monochromatic Al Kα radiation source was used for XPS measurements.

2.2.4 TRANSMISSION ELECTRON MICROSCOPY

Transmission electron microscopy (TEM) was used to determine the particle size and degree of dispersion of samples. TEM uses a highly focused high energy (200kV) electron beam to image samples. The focused electron beam is deflected by atoms as it passes through the sample. The deflected electrons produce an image beneath the sample. Because electron beams can be focused to very small spot size using electromagnetic fields, images with very high resolution (less than 1 nm) can be generated. Particle size and particle dispersion on the carbon support were analyzed with a JEOL 2010F high resolution TEM operated at 200 kV. The TEM images were then analyzed with ImageJ software (NIH) to determine mean particle size and particle size distributions.

2.3 ELECTROCHEMICAL CHARACTERIZATION

2.3.1 Electrode Fabrication

Electrochemical experiments were performed to characterize the electrocatalysts using an Autolab PGSTAT302N potentiostat. In all experiments, the working electrode consisted of catalyst ink deposited on a 5 mm diameter glassy carbon electrode encased

in Teflon. The glassy carbon was polished with 0.05 μm alumina paste before each experiment. All potentials are reported vs. normal hydrogen electrode (NHE).

For electrochemical experiments, the catalyst ink was prepared by mixing 10 mg of catalyst powder with 2 mL of ethanol and 100 μL of 5 wt, % Nafion ionomer solution (Electrochem Inc.) in an ultrasonic bath to form a homogeneous dispersion. 10 μL of ink was then drop cast onto the glassy carbon electrode, dried in air, and then placed under an infrared lamp to remove all traces of solvent. The effective catalyst loading was between 100 and 118 μg metal/cm^2.

2.3.2 Cyclic Voltammetry

Cyclic voltammetry (CV) is a potential sweep technique where the current is recorded as the potential is swept in one direction at a constant rate and then returned to the starting potential at the same rate. Processes occurring at the electrode can be determined from the shape of the voltammogram.

For all CV experiments, the electrolyte was 0.5 M H_2SO_4 solution saturated with nitrogen and scans were performed between 0.05 to 1.2 V vs. NHE at a rate of 20 mV/s. Two types of CV experiments were performed: termed cleaning and stability. Cleaning CV was used to clean the nanoparticle surface and compare features of the catalysts. The potential was swept until a steady scan was observed. For stability testing, thirty CV cycles were run and the hydrogen desorption peak area was calculated for scans six and thirty to estimate the loss of electrochemical surface area. The counter electrode used in both CV tests was a gold mesh. The reference electrode in the cleaning experiments was a saturated calomel electrode (SCE). Its potential is 0.241 V vs. NHE [7]. The reference

electrode used in the stability tests was a mercury/mercury sulfate electrode. Its potential is 0.613 V vs. NHE [7].

2.3.3 Rotating Disk Electrode Experiments

Rotating disk electrode (RDE) is a potential sweep method where the working electrode is a disk rotating at a constant frequency. The mass transfer from the solution to the electrode surface is a well defined function of the rotation rate. Heterogeneous reaction kinetics can be determined from RDE experiments. Since the electrode is rotating at a fast rate, the diffusion boundary layer is very thin and reproducible. Therefore, catalysts can be easily compared.

Two types of RDE experiments were performed to compare the ORR activity of samples. In the first RDE experiment, the electrolyte was 0.5 M H_2SO_4 saturated with oxygen. In the second RDE experiment, the electrolyte solution consisted of 0.1 M methanol and 0.5 M H_2SO_4 to test methanol tolerance. All RDE tests were carried out at 1600 rpm rotation rate sweeping from 0.10 to 1.1 V vs. NHE at a rate of 5 mV/s. The counter electrode was a platinum mesh separated by a porous glass frit and an SCE was the reference electrode.

2.4 SINGLE CELL DIRECT METHANOL FUEL CELL TESTS

Single cell direct methanol fuel cell tests were performed to compare the sample performance in an actual fuel cell environment. Membrane electrode assemblies (MEA) with active area of 5 cm^2 were prepared for single cell DMFC tests for all samples. Commercial carbon cloth (E-Tek LT 1400) was used as both anode and cathode gas diffusion layer (GDL). Nafion 115 (Electrochem Inc) was used as the polymer electrolyte

membrane. A commercial Pt-Ru catalyst supported on carbon with a 60 wt. % metal loading (Alfa Aesar) was used as the anode catalyst. Anode loading for all tests was 2.0 mg metal per cm^2. The catalysts synthesized for this study were used as cathode catalysts with a metal loading of 1.0 mg metal per cm^2.

MEA fabrication consisted of first preparing anode and cathode catalyst inks. Inks consisted of catalyst powder and Nafion ionomer solution added to a water-ethanol mixture. All inks were homogenized in ultrasonic bath. For the anode ink, the catalyst to Nafion weight ratio was 8 : 2 and for the cathodes it was 7 : 3. All inks were transferred to GDL by air-brush. Following ink deposition, MEAs were prepared by hot-pressing a clean proton-exchanged Nafion membrane between catalyst-loaded GDLs at 130 ºC. All MEAs were tested at 80 ºC with 1, 3, and 5 M methanol solution used as fuel, and humidified oxygen at atmospheric pressure as oxidant. MEAs were conditioned by applying an increasing load for at least 4 h until the cell resistance stabilized.

CHAPTER 3

ADDITION OF PLATINUM TO PALLADIUM-COBALT NANOALLOY BY ALLOYING AND GALVANIC DISPLACEMENT

3.1 INTRODUCTION

Yang and co-workers [56, 73, and 74] have recently reported a facile method to decorate the surface of palladium and palladium-alloy nanoparticles with platinum by a galvanic displacement reaction. While this method does not deposit a perfect monolayer of platinum on the catalyst surface as is seen with underpotential deposition of copper monolayer followed by displacement with platinum salt [53], they have observed ORR activity better than commercial platinum catalyst as measured by rotating disk electrode (RDE) and improved methanol tolerance. In this study we used a very similar method to decorate palladium-cobalt alloy catalysts with sub-monolayer platinum skins to study how platinum content affects performance of a DMFC. Instead of starting with a commercial palladium catalyst and using salt impregnation to alloy the cobalt, we prepared a palladium-cobalt alloy by polyol synthesis method. In addition, we performed single fuel cell testing to compare catalyst performance in a direct methanol fuel cell. This allowed us to gauge the benefits of added methanol tolerance above the commercial platinum catalyst that the synthesized catalysts may exhibit. We also prepared platinum-palladium-cobalt alloy catalysts with similar amounts of platinum to compare the influence of near surface platinum to platinum atoms that may be distributed throughout the bulk of the nanoparticle. For the alloy catalysts we modified the same polyol synthesis used above for the palladium-cobalt alloy to include platinum. Both methods,

displacement and alloying with platinum, are expected to increase stability and ORR activity since Pt atoms are more active for ORR and impervious to acid attack at positive potentials. Because Pt is also more active for methanol oxidation, adding Pt should also decrease methanol tolerance. The catalysts were tested by RDE in acidic methanol solution and DMFC single-cell test to investigate the trade-off between improved performance and reduced methanol tolerance.

3.2 EXPERIMENTAL

3.2.1 Displaced Catalyst Synthesis

20 wt% $Pd_{85}Co_{15}$ alloy catalyst supported on carbon black was prepared by a polyol reduction reaction with ethylene glycol as solvent and reducing agent. Water and ethylene glycol were mixed in a 1 : 4 (volume) ratio in a three neck flask. Vulcan XC-72R carbon black (Cabot Corp.) was added to the mixture and thoroughly stirred and mixed in an ultrasonic bath. Then 1.0 M NaOH in ethylene glycol was added dropwise to the flask until a solution pH of 12 was reached. Next, solutions of $CoCl_2 \cdot 6H_2O$ (Alfa Aesar) and Na_2PdCl_4 (Alfa Aesar) in ethylene glycol were slowly dripped into the flask while rapidly stirring. Once the solution was thoroughly mixed, it was rapidly heated in an oil bath under a nitrogen blanket to 180 °C and held for 3 h at that temperature before slowly cooling to room temperature. The contents of the flask were then mixed with water and filtered, washed with deionized water, and dried in a vacuum oven at 65 °C overnight. Following grinding with a mortar and pestle, the powder was heat-treated in a tube furnace under flowing 10 vol. % H_2 in argon. A temperature of 350 °C was maintained for 2 h to alloy the nanoparticles. Platinum was added to the $Pd_{85}Co_{15}$ catalyst

surface by suspending the supported catalyst in a dilute solution of K_2PtCl_4 and heating to 100 °C for 90 min under nitrogen blanket. Finally the displaced catalyst was again filtered and washed with water. Catalysts with two different platinum amounts were prepared for this study by varying the amount of K_2PtCl_4 in the displacement solution. The compositions of the catalyst nanoparticles contained 10 atomic % Pt and 22 % Pt. They are referred to as 10Pt D and 22Pt D respectively. The baseline $Pd_{85}Co_{15}$ catalyst is referred to as $Pd_{85}Co_{15}$. A 20 wt. % platinum on carbon black commercial catalyst (Alfa Aesar HiSPEC 3000) was also used in this study as a comparison. It is referred to as comPt.

3.2.2 Alloyed Catalyst Synthesis

Platinum-palladium-cobalt alloy catalysts with a nominal loading of 20 wt. % on carbon black were prepared by the same method as the palladium-cobalt alloy above except an aqueous solution of H_2PtCl_6 (Strem Chemicals) was added to the flask following the addition of Na_2PdCl_4. The same heat treatment protocol, 2 h at 350 °C under flow of 10 % hydrogen gas was used. Two different alloy catalysts with similar compositions to the displaced catalysts were prepared by varying the amount of H_2PtCl_6 added to the flask. They contained 11 and 22 atom % platinum in the metallic nanoparticles and they are referred to as 11Pt A and 22Pt A.

3.2.3 Materials Characterization

All samples were characterized by XRD, SEM-EDS, TEM, and XPS. The techniques are detailed in Chapter 2. Electrochemical testing consisted of preparing inks and drop-casting the inks onto a glassy carbon working electrode. CV tests were

performed as well as RDE as described in Chapter 2. All catalysts were tested in DMFC single cell tests following the procedure described in Chapter 2.

3.3 RESULTS AND DISCUSSION

3.3.1 Structural and Compositional Characterization

Table 3.1 summarizes the structural and compositional characteristics of the catalysts. The XRD patterns for all of the catalysts studied are shown in Figure 3.1. The displaced catalysts have very similar patterns to the $Pd_{85}Co_{15}$ catalyst. The peaks shift to lower 2θ values as the amount of Pt increases, but the peak widths remain the same. The alloyed Pt-Pd-Co catalysts have slightly smaller lattice parameters than the corresponding displaced catalysts as shown in Figure 3.2. This could be due the presence of a larger fraction of cobalt in the alloy catalysts as measured by EDS. Alloying of Pt with $Pd_{85}Co_{15}$ will increase the lattice parameter because the atomic radius of Pt (0.1385 nm) is greater than both Pd (0.1375 nm) and Co (0.1255 nm) [75].

Table 3.1 Summary of structural and compositional characteristics of catalysts tests

Catalyst	EDS atom ratio Pt : Pd : Co	XPS atom ratio Pt : Pd	Lattice Parameter[a] (nm)	XRD Crystallite Size[b] (nm)	TEM Average Particle Size (nm)
$Pd_{85}Co_{15}$	0 : 85: 15	0 : 100	0.3852	6.5	7
10Pt D	10 : 81 : 9	23 : 77	0.3859	6.4	7
22Pt D	22 : 71 : 7		0.3867	6.3	7
11Pt A	11 : 77 : 12	12 : 88	0.3855	4.4	5
22Pt A	22 : 66 :12		0.3862	3.8	4
comPt	100 : 0 : 0		0.3929	3	

[a] Lattice parameters calculated using (111), (200), (222) and (311) peaks in XRD pattern
[b] XRD particle size estimated using Scherrer equation for (222) peak

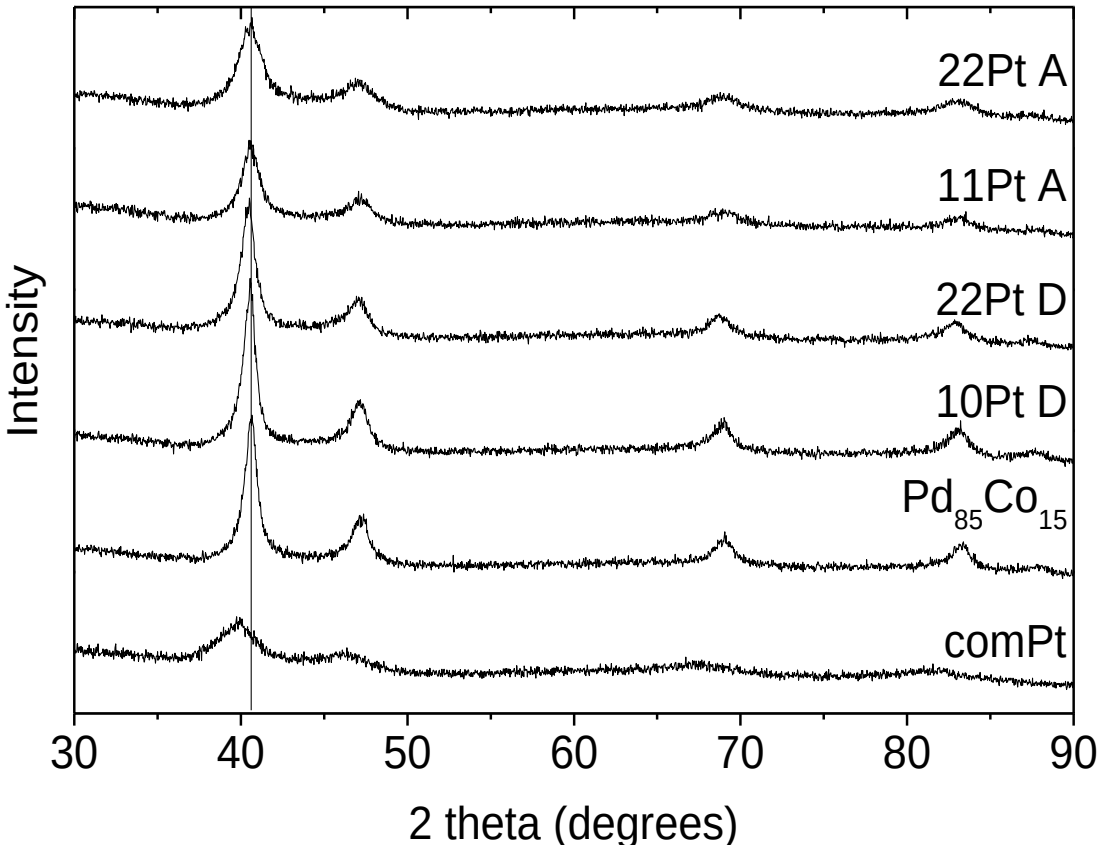

Figure 3.1 XRD patterns of the catalysts tested. All of the catalysts except the comPt catalyst have very similar XRD patterns.

Vegard's law can be used to calculate the lattice parameters for fully alloyed nanoparticles [76]. Performing this calculation shows that the base $Pd_{85}Co_{15}$ catalyst is not fully alloyed; only about 11 atom % of the 15 atom % cobalt in the nanoparticles is alloyed with palladium. Neither the 11Pt A nor the 22Pt A catalyst is fully alloyed according to Vegard's law either, if the calculation is performed with the assumption that platinum and palladium are fully alloyed and the degree of cobalt alloying is variable.

However, they do show a higher degree of cobalt alloying than the $Pd_{85}Co_{15}$ catalyst. For the displaced catalysts, it is not expected or desired that the platinum alloy with the $Pd_{85}Co_{15}$ catalyst. However, the lattice parameters of the 10Pt D and 22Pt D catalysts match the values expected for complete alloying if platinum and the partially alloyed $Pd_{85}Co_{15}$ (11 atom % Co in Pt) are used in the calculation for Vegard's law. This is shown in Figure 3.2 with the solid line that connects the lattice parameter of the $Pd_{85}Co_{15}$ catalyst (0% Pt) with the pure platinum (100% Pt) lattice parameter (not shown in the plot). Both 10Pt D and 22Pt D samples lie directly on this line. Thus, the lattice parameter values indicate alloying of Pt with $Pd_{85}Co_{15}$ even during the displacement reaction. Interfacial alloying in core-shell nanoparticles has also been observed in other systems without an annealing heat treatment [73, 77]. The inter-diffusion driving force is much larger in nanoparticles than at bulk interfaces because the magnitude of the enthalpy of mixing and interfacial energy increase as particle radius decreases [78]. In addition, the diffusion coefficient for atoms near the core-shell interface in a small nanoparticle can be orders of magnitude greater than for atoms in the bulk [78].

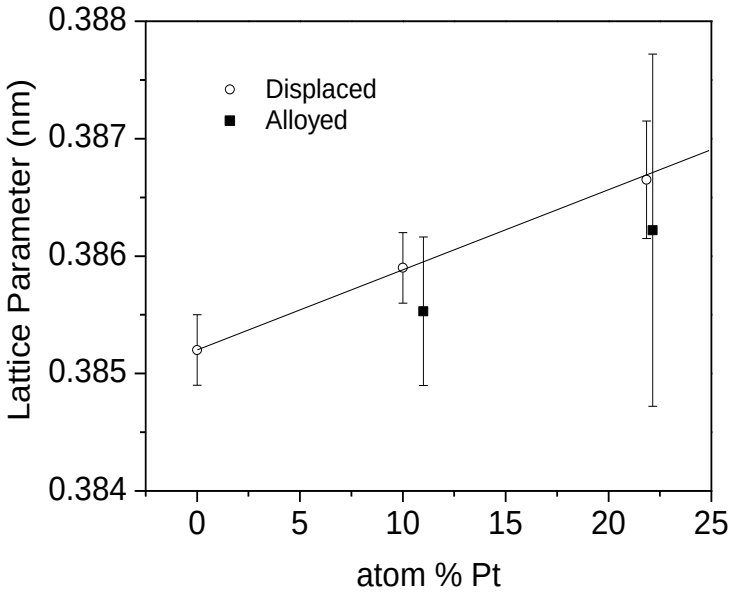

Figure 3.2 Plots of lattice parameter vs. the amount of platinum in the catalyst for the displaced (open circle) and alloyed (solid square) catalysts. Addition of platinum shifts the lattice parameter to larger values in both cases. The black line connects the lattice parameter of the $Pd_{85}Co_{15}$ (0% Pt) with the lattice parameter of Pt (100%). The lattice parameters of both displaced catalysts lie directly on this line.

Particle sizes, as estimated by the Scherrer equation, are reported in Table 3.1 for all the catalysts. The Scherrer equation calculates crystallite size based on XRD peak width. For nanoparticles, it is assumed that each particle consists of a single crystallite [76]. The Pt-Pd-Co alloy catalysts have smaller crystallite sizes than the $Pd_{85}Co_{15}$ or displaced catalysts. Therefore, the addition of H_2PtCl_6 to the polyol process causes smaller nanoparticles to form.

Figure 3.3 (a) and (b) show the TEM images of the displaced samples 10Pt D and 22Pt D respectively. No major difference is observed between the samples, which is expected from the XRD result and the process in which the particles were formed. Both

samples started with the same $Pd_{85}Co_{15}$ base catalysts and relatively small amounts of platinum were introduced by displacement reaction in each case. An estimate of the ratio of surface atoms to total atoms in the base $Pd_{85}Co_{15}$ catalyst shows that the amount of platinum added will not significantly increase the size of the nanoparticles. The amount of atoms on the surface of the $Pd_{85}Co_{15}$ base catalyst can be estimated according to the method of Benfield [79]. If the $Pd_{85}Co_{15}$ nanoparticles are assumed to be cuboctahedron-shaped with an edge length of 3.5 nm (7 nm cross-section length), the percentage of surface atoms is roughly 20 %. Therefore, the amount of platinum added to the 10Pt D catalyst corresponds to enough atoms to replace about half of a monolayer on the base catalyst and the 22Pt D catalyst corresponds to about one monolayer, if platinum is assumed to displace only atoms on the surface. According to this calculation, the particle size would only grow by about 0.5 nm (4 Pt atomic radii) if the platinum plates on the surface instead of displacing atoms in the nanoparticle. This difference is not accurately detectable by either method of particle size analysis employed in this study. It is made clear below with the XPS and EDS results that the platinum is not displacing only atoms on the surface of the nanoparticles, but this should not measurably affect particle size unless the displacement causes pores to form in the nanoparticles. The calculation by Benfield [79] shows that the replacement of 10 or 20% of the atoms in the $Pd_{85}Co_{15}$ catalyst with Pt should have no measureable effect on particle size as was seen by the particle size values from both XRD and TEM.

The TEM images of the alloyed samples 11PtA and 22Pt A are shown in Figure 3.3 (c) and (d), respectively, and the TEM particle size distributions are shown in Figure

3.4 for the four synthesized catalysts. The TEM images show that the nanoparticles are well dispersed on the carbon support in all four samples. TEM size analysis yields slightly larger mean sizes than that estimated by the Scherrer equation as is expected [80]. The two displaced samples also show larger size dispersions even though the same polyol reduction and heat treatment procedure were used. Inclusion of platinum decreases the particle size and may also generate more mono-disperse nanoparticles. However, the smaller particle size of the alloyed nanoparticles does not lead to a significantly larger electrochemical surface area as is seen in the CV results. This could be caused by the relative size distribution skewness of the displaced samples and differences in particle shape.

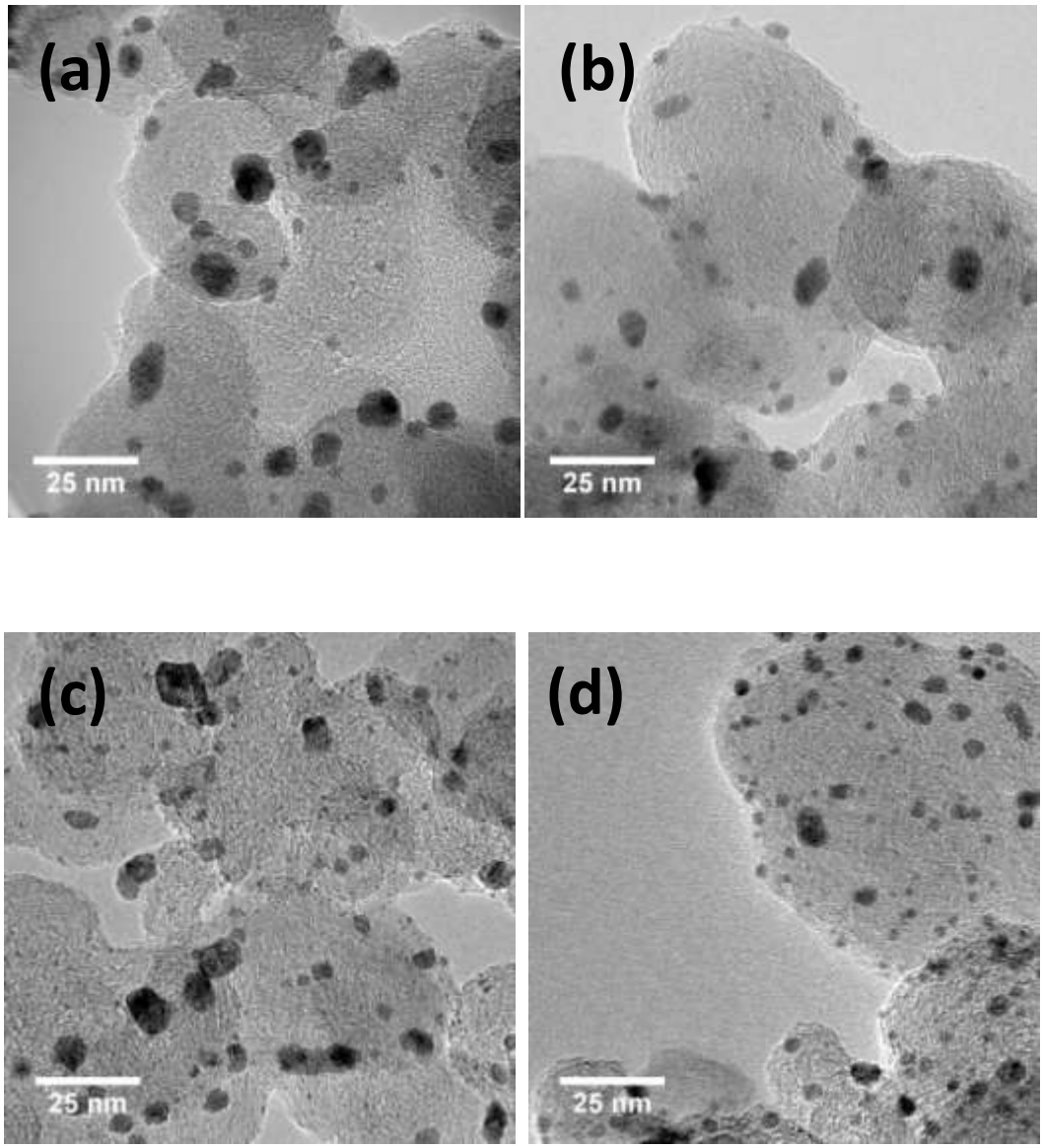

Figure 3.4 TEM images of the catalysts (a) 10Pt D, (b) 11Pt A, (c) 22Pt D, and (d) 22Pt A.

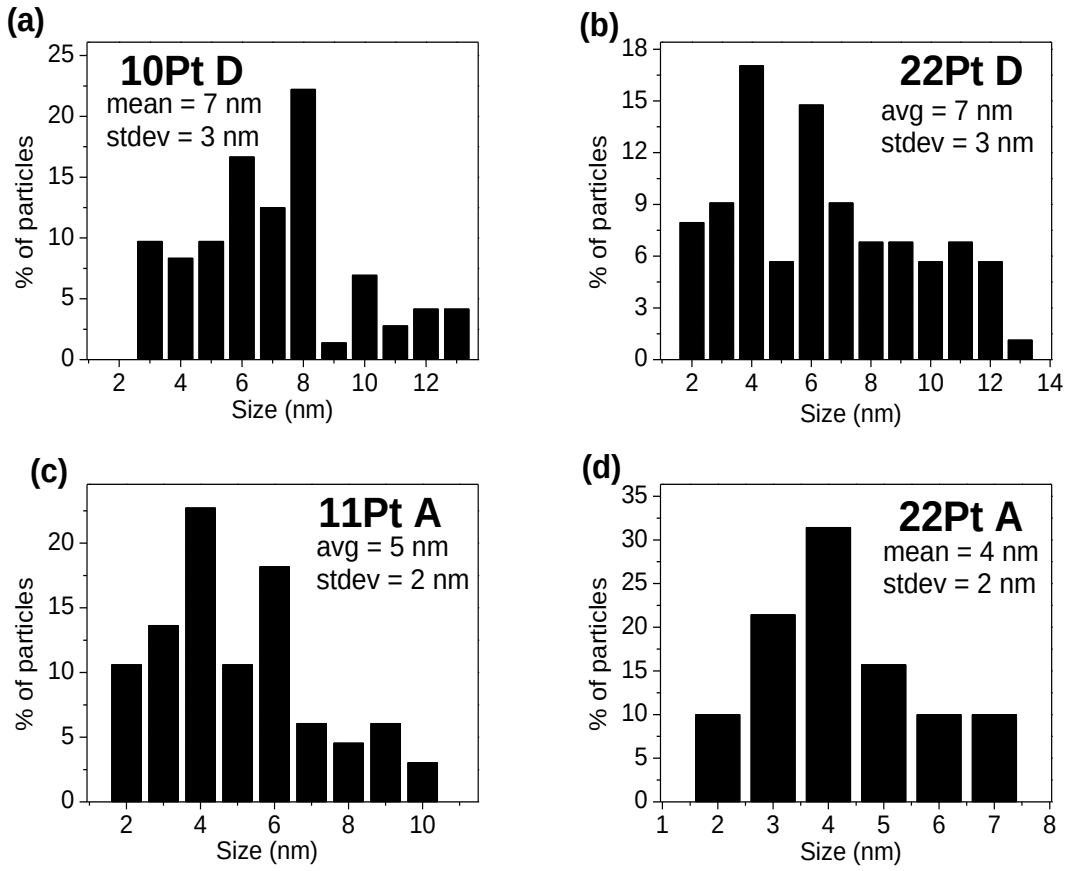

Figure 3.4 Histograms of particle size distributions for (a) 10Pt D, (b) 22Pt D, (c) 11Pt A, and (d) 22Pt A catalysts. Analysis of TEM images using ImageJ software to measure particle size distribution and statistics for each sample are presented in the figure.

EDS results, included in Table 3.1, show that for the two displaced catalysts, K_2PtCl_4 reacts fully in 90 minutes at 100 °C since the platinum content reaches the maximum calculated value. The amount of cobalt is different in the two displaced catalysts because more cobalt is displaced in the 22Pt D sample. In the alloyed catalysts all of the H_2PtCl_6 is also assumed to be reduced completely since Pt^{4+} is easily reduced under the conditions employed (ethylene glycol reducing agent at 180 ºC). The amount of

cobalt in the alloyed nanoparticles is slightly less than that expected based on the nominal composition $Pd_{85}Co_{15}$. It has been suggested that cobalt precipitates as a hydroxide in the basic ethylene glycol solution and acts as a seed for the reduction of the noble metals [81]. If this is the case, the addition of acidic H_2PtCl_6 may lower the pH of the solution, preventing more Co ions from precipitating throughout the polyol reduction.

XPS data were collected for the $Pd_{85}Co_{15}$, 10Pt D, and 11Pt A samples. The Pt 4f regions are shown for the 10Pt D and 11Pt A catalysts in Figure 3.5. The Pd 3d regions are shown for the $Pd_{85}Co_{15}$, 10Pt D, and 11Pt A catalysts in Figure 3.6. The XPS compositions given in Table 3.1 were calculated by the Kratos software. Shirley's method was used to remove the background, and then the overall peak areas in the Pt 4f and Pd 3d regions were calculated. The peak areas were multiplied by photo-ionization cross-sections for Pt 4f and Pd 3d to determine, respectively, the relative amounts of Pt and Pd. In all XPS trials, very little signal was observed for Co, even though the XPS sampling depth is expected to be similar to the radius of the nanoparticles. This result could be due to the low concentration of Co in the sample and low or little Co near the surface. In addition, cobalt is expected to be concentrated near the center of the nanoparticles, which would further diminish its signal. Based on relative surface energies, palladium and platinum will preferentially segregate to the nanoparticle surface with respect to cobalt during heat treatment in reducing atmosphere [82]. It is apparent from the EDS data that cobalt is being removed from the catalyst during displacement. This implies that some cobalt atoms are near the surface or move there during the displacement reaction.

Comparing the ratio of platinum to palladium XPS signals between 10Pt D and 11Pt A, the platinum concentration is about double in the displaced catalyst. For the 11Pt A sample the Pt : Pd ratios measured by EDS and XPS are very similar. Since the XPS signal decays exponentially as a function of sample depth, platinum atoms are concentrated closer to the surface in the displaced catalyst than the alloyed catalyst.

A comparison of standard electrochemical reduction potentials (1.1188 V for Pt^{2+}, 0.915 V for Pd^{2+} and -0.277 V for Co^{2+} [7]) shows that Pt^{2+} should displace both metallic Co and Pd, the driving force being much greater for Co than Pd. In addition, the Pd^{2+} ions formed from displacement by platinum can also easily displace metallic cobalt atoms. The mechanism of displacement is unclear especially since there are oxidized species on the surface and the near surface concentration of cobalt is expected to be very low. The EDS results verify that cobalt is preferentially displaced since the palladium to cobalt ratio decreases following the displacement step in both displaced samples.

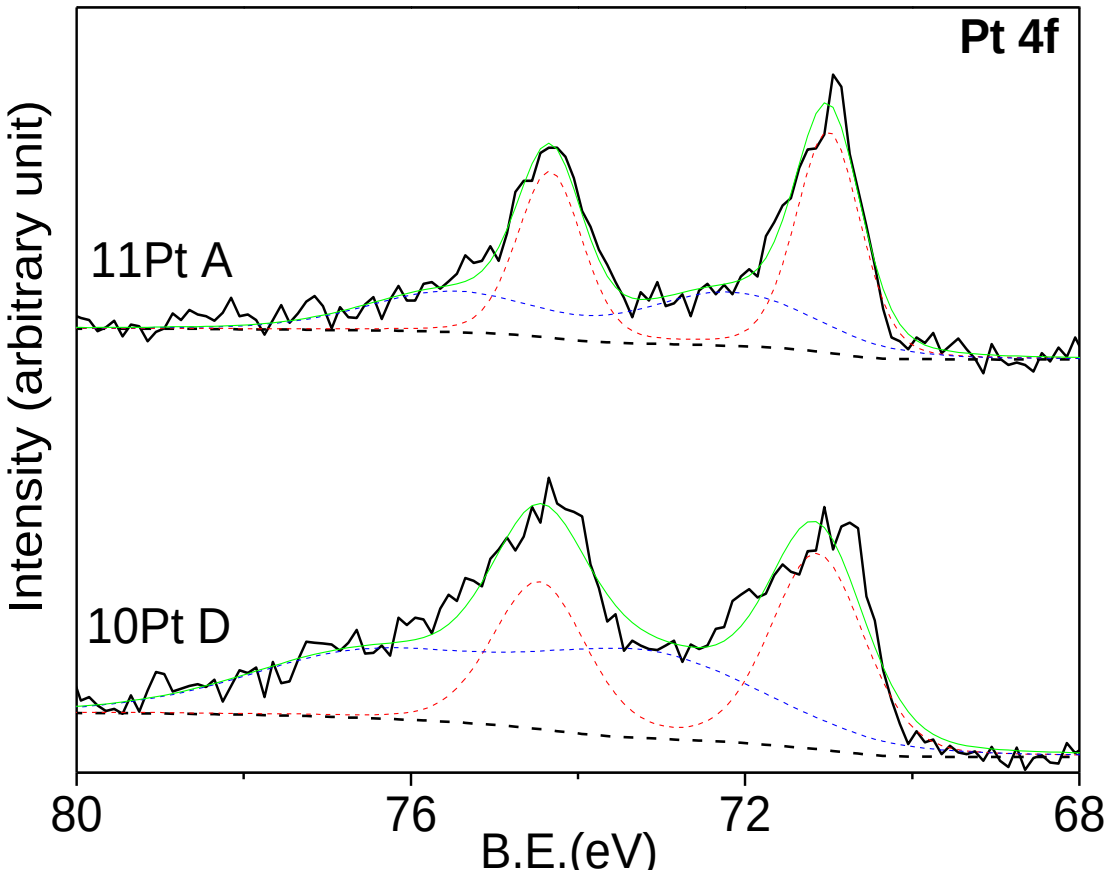

Figure 3.5 XPS spectrum for the 10Pt D and 10Pt A catalysts in the Pt 4f region. The background was fit with Shirley's method (dashed black line). The dashed red line corresponds to the metallic peak, the dashed blue line corresponds to the oxide peak, and the green line is the sum of the oxide and metallic peaks.

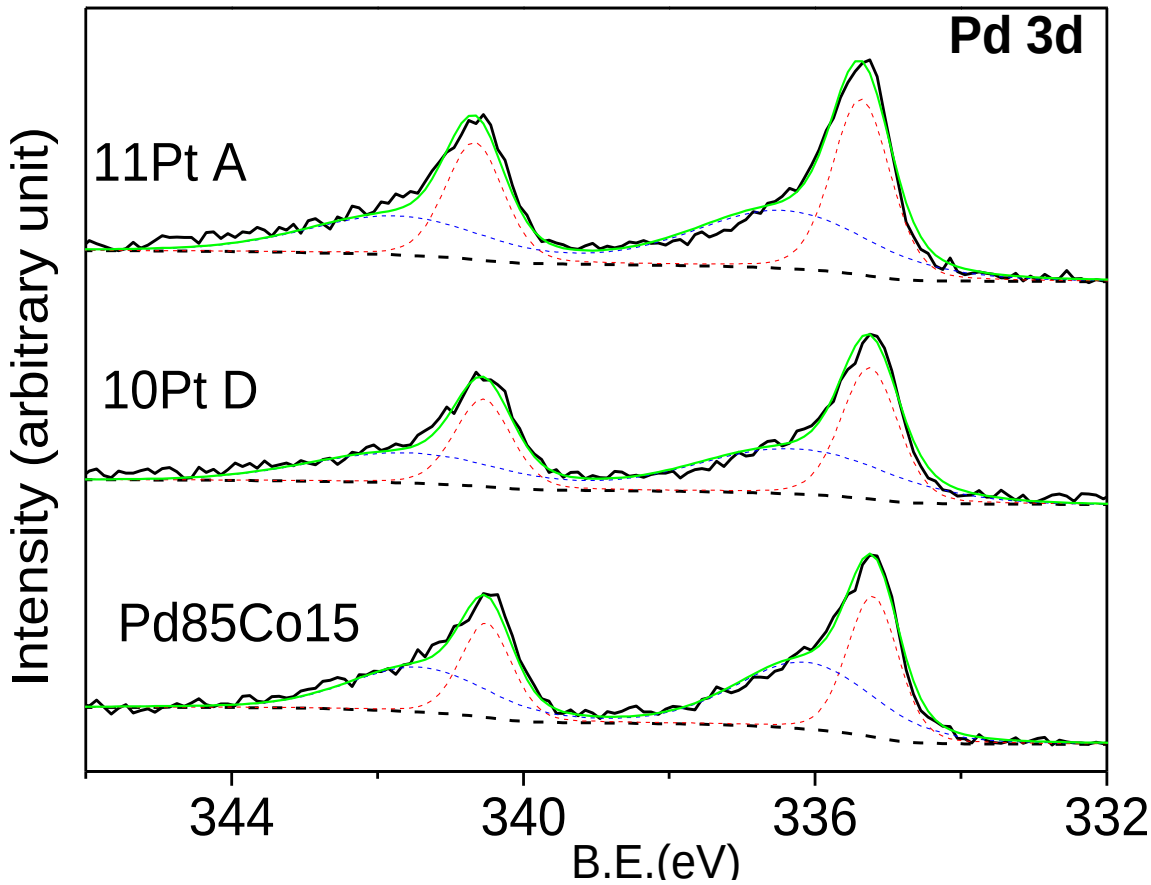

Figure 3.6 XPS spectrum for the $Pd_{85}Co_{15}$, 10Pt D and 10Pt A catalysts in the Pd 3d region. The background was fit with Shirley's method (dashed black line). The dashed red line corresponds to the metallic peak, the dashed blue line corresponds to the oxide peak, and the green line is the sum of the oxide and metallic peaks.

3.3.2 Electrochemical Characterization

The cyclic voltammograms are presented in Figure 5 (a) with a close-up of the oxide reduction peaks shown in Figure 5 (b). The electrochemical surface area (ECSA) cannot be accurately calculated from the hydrogen desorption peak (anodic 0-0.3V vs. NHE) area for Pd containing catalysts because of hydrogen absorption into Pd, but since all catalysts (except comPt) contain similar amounts of Pd, the hydrogen peak area and

oxide reduction peak can be used to roughly compare ECSA among catalysts. It is apparent from the CVs that the comPt catalyst has a much larger ECSA than all of the synthesized catalysts. This is expected because all of the synthesized catalysts have particle sizes larger than the comPt catalyst. The platinum alloy catalysts have smaller particle sizes than the displaced catalysts, but their voltammograms do not reflect a larger ECSA. The 22Pt D catalyst displays the largest hydrogen desorption current among the synthesized catalysts, but its metal loading is also about 20% greater than the alloy catalysts. The particle shape and surface roughness may account for the ECSA discrepancy between alloyed and displaced catalysts. In general, the addition of Pt to the $Pd_{85}Co_{15}$ catalyst has a large effect on the shape of the hydrogen desorption and oxide reduction peaks as shown in Figure 3.7. The hydrogen desorption regions are much smoother for the displaced and alloy catalysts than the $Pd_{85}Co_{15}$ catalyst. The alloy and displaced catalysts show the same trend with a spike around 0.01 V vs. NHE and a smooth peak centered near 0.18 V. The oxide reduction peak broadens and shifts to more positive potentials for the Pt containing catalysts than the $Pd_{85}Co_{15}$ catalyst as seen in Figure 3.7 (b). The peak shift is less dramatic in the alloy catalysts than in the displaced catalysts, but the trend is the same, *i.e.* increasing the Pt content shifts the peak to a more positive potential similar to comPt.

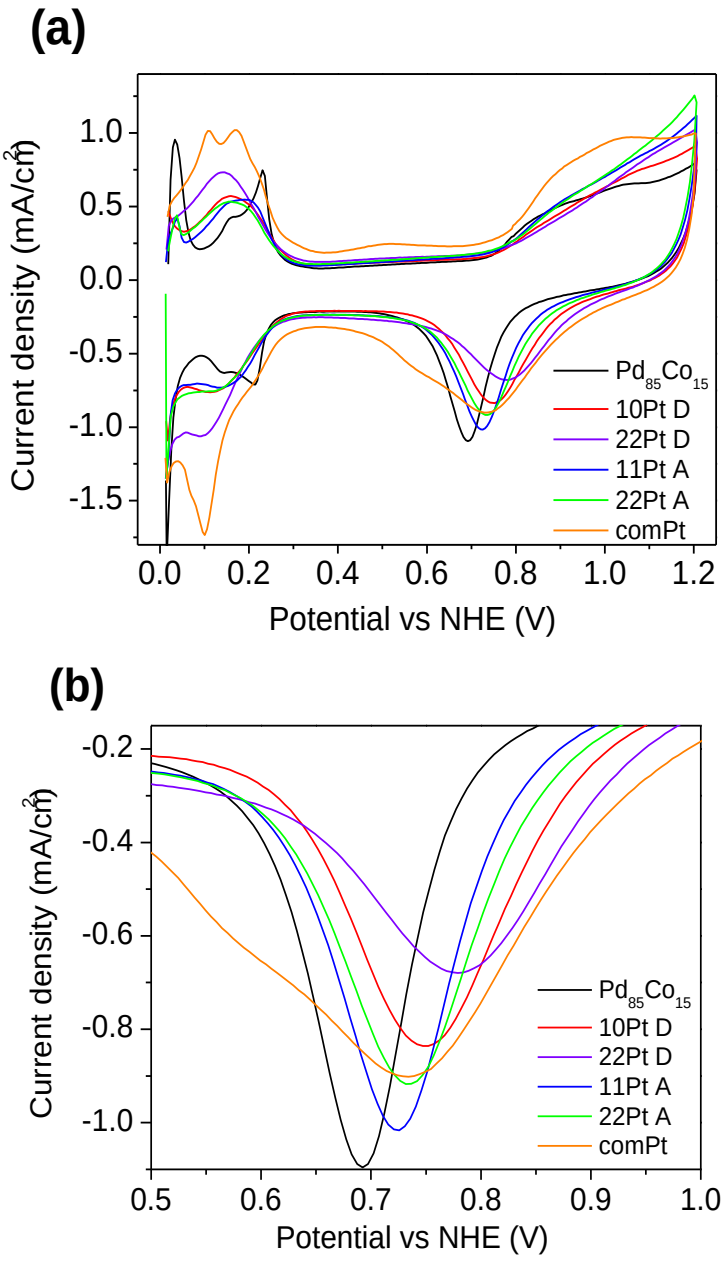

Figure 3.7(a) Cyclic voltammograms of comPt, $Pd_{85}Co_{15}$, 10Pt D, 22Pt D, 11Pt A, and 22Pt A catalysts. The data were collected in nitrogen-purged 0.5 M H_2SO_4 solution at room temperature with a scan rate of 50 mV/s. (b) Close-up of oxide reduction region of CV showing the variation of peak oxide reduction potential among catalysts.

The RDE plot in Figure 3.8 shows the trend in ORR activity of the catalysts. The comPt has the smallest overpotential followed by 22Pt D. The 10Pt D, 11Pt A, and 22Pt A catalysts show very similar performance, while $Pd_{85}Co_{15}$ is the least active catalyst. Adding Pt to the $Pd_{85}Co_{15}$ catalyst by displacement or alloying improves its ability to catalyze the ORR in acid. It is interesting to note that the 22Pt A and 11Pt A catalysts showed very similar performances. It was expected that a higher fraction of Pt would lead to improved ORR kinetics since platinum sites are more active than palladium sites in acid electrolyte.

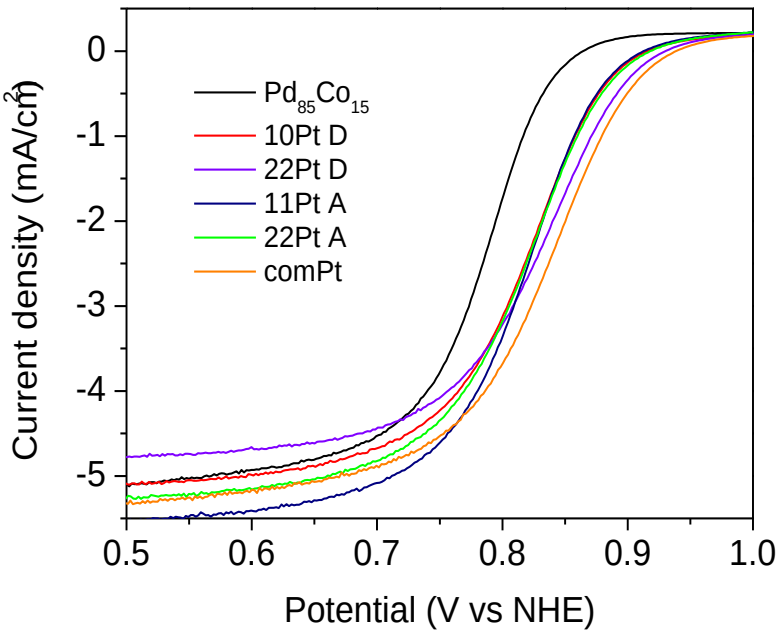

Figure 3.8 Hydrodynamic polarization curves of studied catalysts collected at room temperature in oxygen-saturated 0.5M H_2SO_4 solution

Figure 3.9 compares the mass specific ORR activities at 0.9 V vs. NHE. The $Pd_{85}Co_{15}$ catalyst is not included because its onset potential is less than 0.9 V. The plot

shows that the displaced catalysts have a higher activity on a metal and a platinum metal basis than the alloy catalyst. The 22Pt D sample showed the largest current at 0.9 V of all the catalysts on a platinum basis. While increasing the platinum content increases the platinum specific activity for the displaced catalysts, the opposite trend is observed in the alloy catalysts. This can be explained by the relative number of surface Pt sites in the alloy catalysts. Increasing the Pt alloy content does not necessarily increase the amount of surface Pt sites. On a Pt + Pd basis, the comPt catalyst still shows the highest ORR activity.

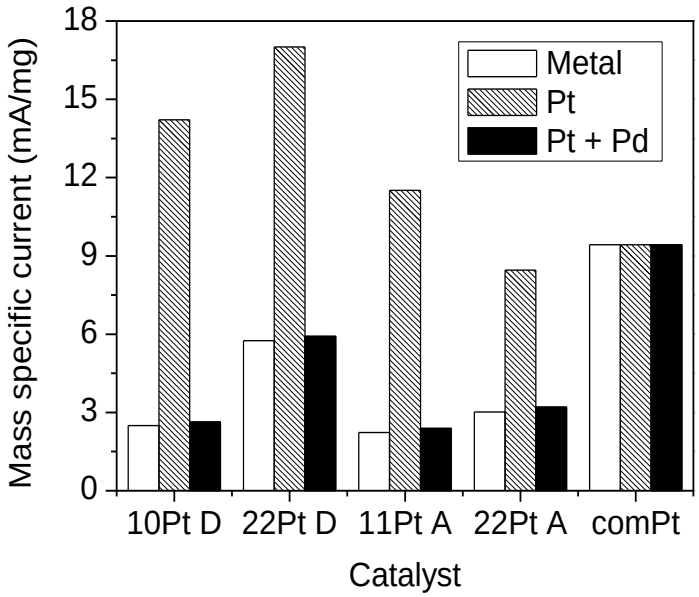

Figure 3.9 Mass specific current densities calculated from the RDE tests at 1600 rpm rotation rate measured per unit mass of total metal, platinum metal, and noble metal in methanol-free electrolyte at 0.90 V vs. NHE.

Figure 3.10 displays the methanol tolerance of the catalysts measured by performing RDE in 0.1 M methanol + 0.5M H_2SO_4 solution. The trend is reverse of the

RDE result above; the comPt catalyst is so greatly affected by methanol that it gives a positive (anodic) current at all potentials shown in the plot. The 22Pt D sample is the least methanol tolerant among the catalyst samples synthesized in this study. The 10Pt D, 22Pt A and 11Pt A catalysts are much more inert to methanol, as is the $Pd_{85}Co_{15}$ catalyst. Figure 3.11 compares the specific ORR current for the catalysts at 0.85 V. The comPt catalyst is not included. The 10Pt A catalyst shows the highest ORR current on all bases. On a metal basis and a Pt + Pd basis, the 22Pt A catalyst performs slightly better than the 10Pt D catalyst.

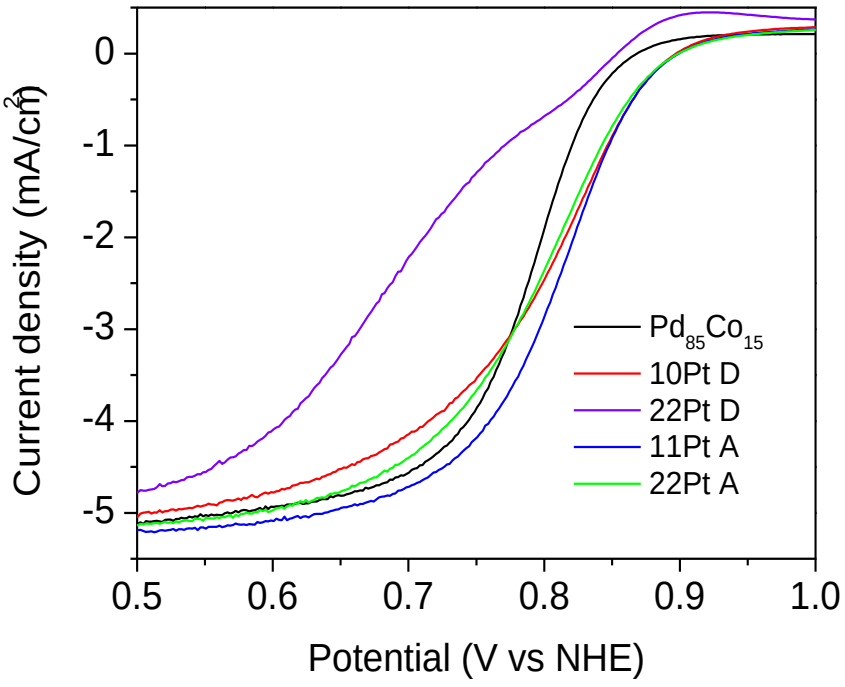

Figure 3.10 Hydrodynamic polarization curves of the catalysts, collected at room temperature in oxygen-saturated 0.5M H_2SO_4 solution.

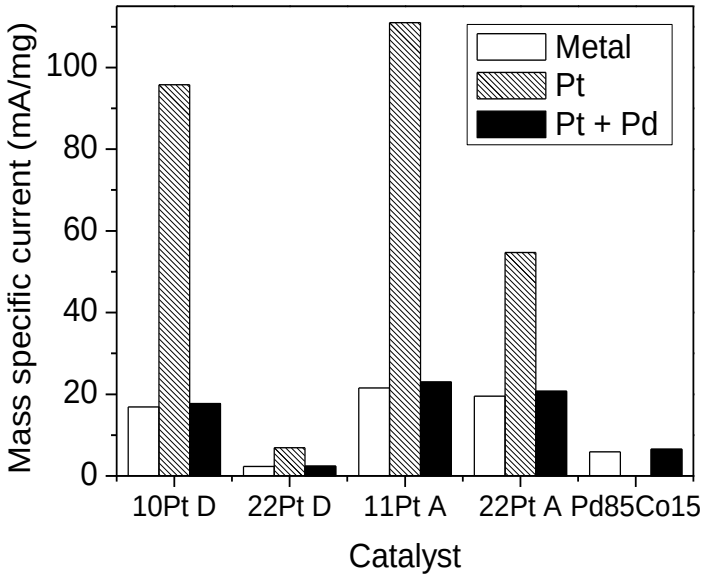

Figure 3.11 Mass specific current densities calculated from the RDE tests in 0.1M methanol at 1600 rpm rotation rate measured per unit mass of total metal, platinum metal, and noble metal in methanol-free electrolyte at 0.90 V vs. NHE.

Table 3.2 contains the results of the accelerated catalyst stability test. The stability was estimated by measuring the area under the hydrogen desorption regions after 6 and 30 CV scans and the percent loss in area is reported. This stability test does not exactly mimic actual fuel cell operating conditions because the potential is scanned to 1.2 V vs. NHE, but it does accelerate the loss of surface area and each catalyst is submitted to identical treatment. An Hg/Hg_2SO_4 reference electrode was used in the test to eliminate any influence of chloride ions. The results show that the addition of the more-noble Pt atoms to the $Pd_{85}Co_{15}$ catalyst dramatically increases the stability of the nanoparticle catalyst in all cases. The 22Pt A catalyst showed slightly less ECSA loss than the 10Pt D and 22Pt D catalysts. However this difference is within the accuracy of the method used,

so it cannot be concluded that the 22Pt A catalyst is the most durable. The 11Pt A ECSA loss was double that of the other Pt containing catalysts except comPt. The comPt catalyst performed worse in the stability test than the Pt decorated catalysts because of the difference in nanoparticle size. The sub-3 nm platinum particles are much more susceptible to coarsening than the larger particles [83]. A stability test cycling the potential between 0.6 and 0.8V vs. NHE could give more distinguishing durability results since this range of potentials is actually seen in an operating fuel cell. Since the catalysts are relatively stable, a test of this type was not practical.

Table 3.2 Loss of electrochemical surface area as measured after 30 CV scans between 0 and 1.2 V vs. NHE. Surface area measured from hydrogen desorption peak of scans 6 and 30.

Sample	**ECSA Loss**
$Pd_{85}Co_{15}$	48%
10Pt D	10%
22Pt D	10%
11Pt A	18%
22Pt A	8%
comPt	15%

The electrochemical tests show the relationship between platinum content, ORR activity, methanol tolerance, and catalyst stability. Adding more platinum to the particle increases ORR activity and catalyst stability, but decreases methanol tolerance. Adding the platinum to the surface increases the ORR activity more than alloying, but does not

appear to further increase the stability at the 20 atom % Pt composition. Because of the trade-off between ORR activity and methanol tolerance, actual fuel cell tests should show the best performing catalyst in a DMFC.

3.2.3 Fuel Cell Tests

The single cell test results are shown in Figures 3.12-3.14 for 1 M, 3 M and 5 M methanol anode feed, respectively. The results at all three methanol concentrations mirror the RDE results in Figure 3.8. The 22Pt D catalyst performs very similarly to the comPt catalyst at all methanol concentrations tested. The 22Pt A, 11Pt A and 10Pt D samples show similar performance. More variability is expected in the single-cell tests because of more variables involved in single cell including spraying catalyst inks, hot pressing, and cell conditioning. The results show that methanol cross-over is not a significant issue at 1, 3, or 5M methanol concentration in the feed to the anode because the least methanol tolerant catalysts perform best at all three test conditions. Increasing the methanol concentration from 1 to 3 M increases the overall performance of the fuel cells, but increasing the methanol concentration in the fuel from 3 to 5M slightly decreases the performance for all catalysts. The performance decrease is most likely due to added resistance from membrane swelling, not methanol cross-over to the cathode since the trend is the same for all catalysts regardless of methanol tolerance. Methanol permeation into a Nafion membrane increases with increasing temperature and increasing methanol concentration at the anode [25]. The increase of methanol in the membrane will decrease energy efficiency regardless of methanol tolerance. Cathode methanol tolerance is not

critical at the operating conditions tested in this study. The overall cell performance trend does not change at 1, 3, or 5 M methanol feed.

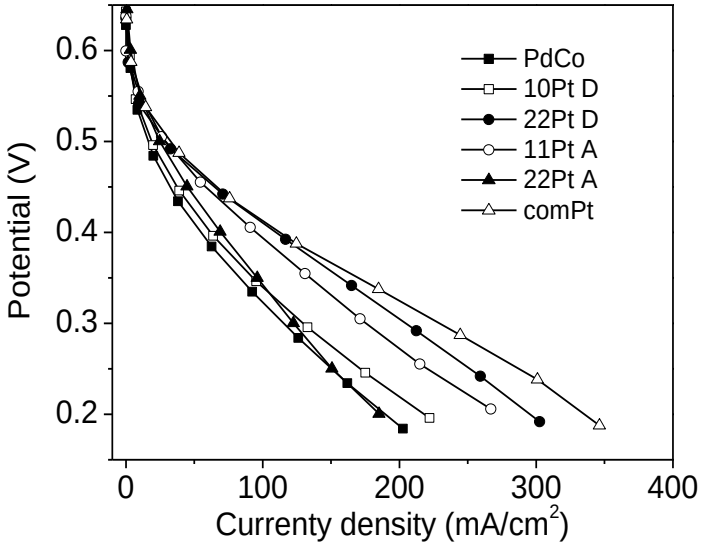

Figure 3.12 Polarization curves for single cell DMFC tests with 1 M methanol fuel at 80 °C.

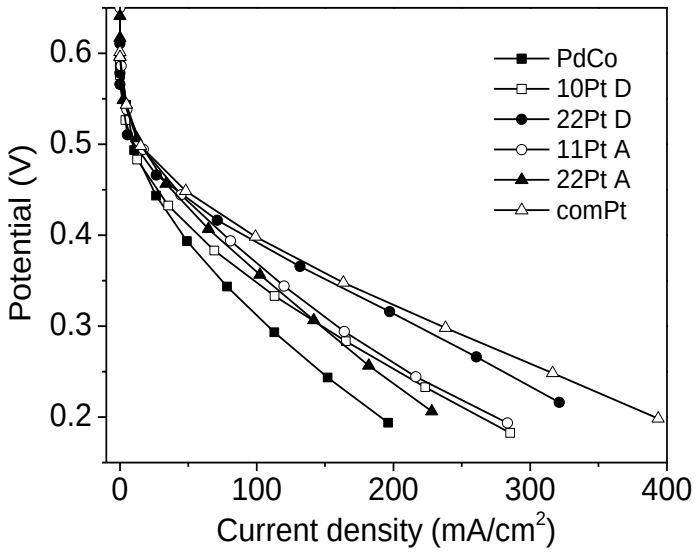

Figure 3.13 Polarization curves for single cell DMFC tests with 3 M methanol fuel at 80 °C.

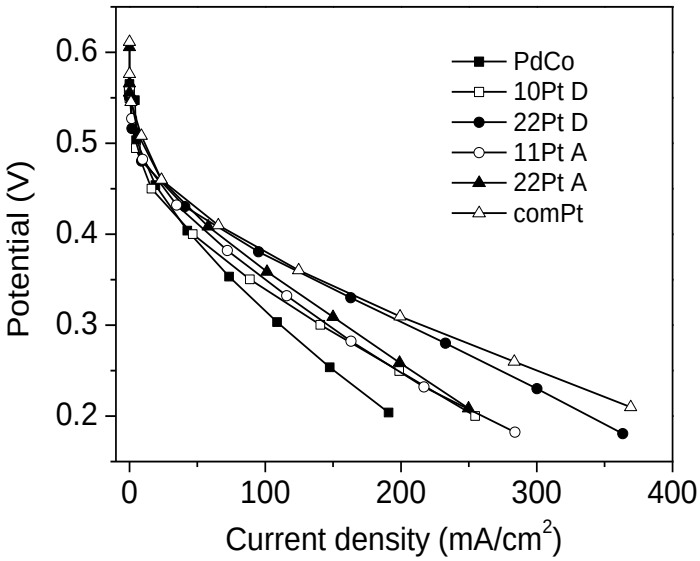

Figure 3.14 Polarization curves for single cell DMFC tests with 5 M methanol fuel at 80 °C.

3.3 CONCLUSIONS

The addition of platinum to a palladium-cobalt alloy catalyst by either alloying the platinum with palladium and cobalt or adding platinum to the nanoparticle by galvanic displacement was found to improve ORR activity and enhance stability against nanoparticle dissolution. Galvanic displacement was found to increase ORR activity more than alloying even though alloying generates a smaller catalyst nanoparticle. Galvanically displaced catalysts were also found to be less tolerant to methanol. These results are consistent if the galvanic displacement catalysts contain more platinum surface sites than the corresponding alloy catalysts because platinum sites are more active for ORR and methanol oxidation than palladium sites. While it is difficult to measure the surface composition of nanoparticles, the XPS measurements and cyclic voltammograms seem to support this conclusion. The displaced catalyst probed with XPS showed a platinum to palladium ratio twice as large as the corresponding alloy catalyst. The CV results for the displaced catalysts showed more platinum-like characteristics than alloyed catalysts.

The XRD results show lattice parameter increases after platinum displacement. This means that all platinum atoms do not remain on the surface of the nanoparticles. In addition, cobalt is preferentially displaced relative to palladium. Further work is necessary to understand the displacement step in the experiment because of these interesting results.

DMFC tests with 1, 3, and 5 M methanol showed similar results to the RDE tests, but the increased methanol-tolerance of the platinum-palladium-cobalt catalysts did not

enhance their performance in comparison to commercial platinum catalyst. Thus, methanol cross-over had little effect on the fuel cell performance at the operating conditions used in this study.

References

[1] K. Kordesh and G. Simader, *Fuel Cells and their Applications*, VCH, 1996.

[2] U. Eberle and R. von Helmolt, Energy Environ. Sci., 3, 689 (2010).

[3] B. C. H. Steele and A. Heinzel, Nature, 414, 345 (2001).

[4] G. F. McLean, T. Niet, S. Prince-Richard and N. Djilali, Int. J. Hydrogen Energy, 27, 507, (2002)

[5] S. M. Haile, C.R.I. Chisholm, K. Sasaki, D.A. Boysen and T. Uda, Faraday Discuss., 134, 17 (2007).

[6] H. A. Gasteiger, N. Markovic, P.N. Ross and E.J. Cairns, J. Phys. Chem., 97, 12020 (1993).

[7] A. J. Bard, L. R. Faulkner, Electrochemical Methods Fundamentals and Applications, second ed., Wiley, 2001.

[8] K. B. Oldhan and J. C. Myland, *Fundamentals of Electrochemical Science*, Academic Press Inc., San Diego, USA, 1994

[9] J. S. Newman and K. E. Thomas-Alyea, *Electrochemical Systems*, John Wiley & Sons, Inc., Hoboken, New Jersey. 2004.

[10] R. O'Hayre, S. Cha, W. Colella and F.B. Prinz, Fuel Cell Fundamentals, John Wiley & Sons, Inc., Hoboken, New Jersey. 2006.

[11] J. Larminie and A. Dicks, *Fuel Cell Systems Explained*, John Wiley & Sons, Chichester, 2001

[12] A. S. Arico, V. Baglio and V. Antonucci, Direct Methanol Fuel Cells: History, Status , and Perspectives, in J. Zhang and H. Liu (eds.), Electrocatalysis of Direct Methanol Fuel Cells: From Fundamentals to Applications, Wiley VCH, Weinheim, 2009.

[13] K. T. Adjemian, S. J. Lee, S. Srinivasan, J. Benziger, A. B. Bocarsly, J. Electrochem. Soc., 149, A256 (2002).

[14] A.S. Arico, S. Srinivasan and V. Antonucci, Fuel Cells, 1, 133 (2001).

[15] S. Wasmus and A. Kuver, J. Electroanal., Chem., 461, 14 (1999).

[16] I. Honma and T. Toda, J. Electrochem. Soc., 150, A1689 (2003).

[17] S. Mukerjee, S. J. Lee, E.A. Ticianelli, J. McBreen, B. N. Grgur, N. M. Markovic, P. N. Ross, J.R. Giallombardo and E. S. De Castro, Electrochem. Solid-state Lett., 2, 12, (1998).

[18] C. Roychowdhury, F. Matsumoto, V. B. Zeldovich, S. C. Warren, P. F. Mutolo, M. J. Ballesteros, U. Wiesner, H. D. Abruna and F. J. DiSalvo, Chem. Mat., 18, 3365 (2006).

[19] K. Drew, G. Girishkumar, K. Vinodgopal and P. V. Kamat, J. Phys. Chem. B, 109, 11851 (2005).

[20] J. Lee, S. Han, Y. Song, J. Kim, B. Roh, I. Hwang, W. Choi and K. Park, App. Catal. A: General 375, 149 (2010).

[21] C. L. Campos, C. Roldan, M. Aponte, Y. Ishikawa and C. R. Cabrera, J. Electroanal Chem., 581, 206 (2005).

[22] C. Xu, R. Zeng, P. K. Shen and Z. Wei, Electrochim. Acta, 51, 1031 (2005).

[23] M. A. Hickner, H. Ghassemi, Y. S. Kim, B. R. Einsla, and J. E. McGrath , Chem. Rev., 104, 4587 (2004).

[24] P. Colomban (Ed.), Proton Conductors: Solids, Membranes and Gels-Materials and Devices (Chemistry of Solid State Materials, No 2), Cambridge University Press, 1992.

[25] X. Ren, T. E. Springer, T. A. Zawodzinski and S. Gottesfeld, J. Electrochem. Soc., 147, 466 (2000).

[26] W. Vielstich, A. Paganin and F. H. B. Lima, E. A. Ticianelli, J. Electrochem. Soc., 148, A502 (2001).

[27] S. Z. Ren, G. Q. Sun, C. N. Li, Z. X. Liang, Z. M. Wu, W. Jin, Q. Xin, and X. F. Yang, J. Membr. Sci., 282, 450 (2006).

[28] L. J. Hobson, H. Ozu, M. Yamaguchi, and S. Hayasea, J. Electrochem. Soc., 148, A1185 (2001).

[29] J. T. Wang, S. Wasmus, and R. F. Savinell, J. Electrochem. Soc., 143, 1233 (1996).

[30] K. D. Kreuer, J. Membr. Sci., 185, 29 (2001).

[31] W. Li, A. Bellay, Y. Z. Fu, and A. Manthiram, J. Power Sources, 180, 719 (2008).

[32] J. K. Lee, W. Li, A. Manthiram, and M. D. Guiver, J. Electrochem. Soc., **156**, B46 (2009)

[33] K. J. J. Mayrhofer, B. B. Blizanac, M. Arenz, V. R. Stamenkovic, P. N. Ross and N. M. Markovic, J. Phys. Chem. B, 109, 14433 (2005).

[34] J. X. Wang, N.M. Markovic and R. R. Adzic, J. Phys. Chem. B, 108, 4127 (2004).

[35] J. K. Norskov, J. Rossmeisl, A. Logadottir, L. Lindqvist, J. R. Kitchin, T. Bliggard and H. Jonsson, J. Phys. Chem. B, 108, 17886 (2004).

[36] H. Wroblowa, Y. C. Pan and J. Razumney, *J. Electroanal. Chem.,* **69**, 195 (1976).

[37] N. M. Markovic, T. J. Schmidt, V. Stamenkovic, and P. N. Ross, *Fuel Cell*s, **1**, 105 (2001).

[38] D. E. Curtin, R.D. Lousenberg, T. J. Henry, P. C. Tangeman and M. E. Tisack, J. Power Sources, 131, 41 (2004).

[39] N. M. Markovic, R.R. Adzic, B. D. Cahan and E. B. Yeager, J. Electoanl. Chem., 377, 249 (1994).

[40] C. Koenigsmann, W. Zhou, R.R. Adzic, E. Sutter and S. S. Wong, Nano Lett., 10, 2806, (2010).

[41] L. Tang, B. Han, K. Persson, C. Friesen, T. He, K. Sieradzki and G. Ceder, J. Am. Chem. Soc., 132, 596 (2010).

[42] B. Gurau and E. S. Smotkin, J. Power Sources, 112 339 (2002).

[43] B. E. Tonn, S. Das, Trans. Res. Record, 1815, 99-104 (2002)

[44] H. Yang, N. Alonso-Vante, J. M. Leger and C. Lamy, J. Phys. Chem. B, 108, 1938 (2004).

[45] E. Antolini, R. R. Passos and E. A. Ticianelli, Electrochim. Acta, 48, 263 (2002).

[46] A. K. Shukla, R. K. Raman, N. A. Choudhury, K. R. Priolkar, P. R. Sarode, S. Emura, and R. Kumashiro, J. Electroanal. Chem., 563 181 (2004).

[47] V. R. Stamenkovic, B. Fowler, B. S. Mun, G. Wang, P. N. Ross, C. A. Lucas, N.M. Markovic, Science, 315, 493 (2007).

[48] S. Mukerjee and S. Srinivasan, J. Electroanal. Chem., 357, 201 (1993).

[49] J. R. Kitchin, J. K. Norskov, M. A. Barteau and J. G. Chen, J. Chem. Phys., 120, 10240 (2004).

[50] F. Maillard, L. Dubau, M. Chatenet, J. Andre and E. Rossinot, Electrochem. Comm., 12, (2010).

[51] S. Koh and P. Strasser, J. Am. Chem. Soc., 129, 12624, (2007).

[52] J. Zhang, M. B. Vukmirovic, K. Sasaki, A. U. Nilekar, M. Mavrikakis and R.R. Adzic, J. Am. Chem. Soc., 127, 12480 (2005).

[53] R. R. Adzic, J. Zhang. K. Sasaki, M. B. Vukmirovic, M. Shao, J.X. Wang, A.U. Nilekar, M. Mavrikakis, J. A. Valerio and F. Uribe, Top. Catal., 46, 249 (2007).

[54] V. Mazumder, M. Chi, K.L. More and S. Sun, J. Am. Chem. Soc., 132, 7848 (2010).

[55] C. Wang, D. van der Vliet, K. L. More, N. J. Zaluze, S. Peng, S. Sun, H. Daimon, G. Wang, J. Greeley, J. Pearson, A. P. Paulikas, G. Karapetrov, D. Strmcnik, N. M. Markovic and V. R. Stamenkovic, Nano Letters, 2010, DOI: 10.1021/nl102369k

[56] J. Yang, W. Zhou, C. H. Cheng, J.Y. Lee and Z. Liu, ACS Appl. Mater. Interfaces, 2, 119 (2010).

[57] H. Liu, A. Manthiram, Electrochem. Commun., 10, 740 (2008).

[58] M. Shao, P. Liu, J. Zhang and R. R. Adzic, J. Phys. Chem. B, 111, 6772 (2007).

[59] M. H. Shao, K. Sasaki, and R. R. Adzic, *J. Am. Chem. Soc*., **128**, 3526(2006).

[60] J. Zhao, A. Sarkar, and A. Manthiram, *Electrochim. Acta,* **55**, 1756 (2010).

[61] N. N. Kariuki, X. Wang, J. R. Mawdsley, M. S. Ferrandon, S.G. Niyogi, J. T. Vaughey and D. J. Meyers, Chem. Mat., 22, 4144 (2010).

[62] V. Raghuveer, P. J. Ferreira, A. Manthiram, *Electrochem. Commun* .**8**, 807 (2006).

[63] A. Sarkar, A. Vadivel Murugan, and A. Manthiram, *J. Mat. Chem.*, **19**, 159 (2009)

[64] H. Liu, A. Manthiram, Energy Environ. Sci., 2, 124 (2009).

[65] R. Jasinski, *Nature*, **201**, 1212 (1964).

[66] M. Lefevre, E. Proietti, F. Jaouen and J. Dodelet, Science, 324, 71 (2009).

[67] N. Alonso Vante, H. Tributsch, Nature, 323, 431 (1986).

[68] K. Lee, L. Zhanag and J. Zhang, J. Power Sources, 165, 108 (2007).

[69] H. Zhong, H. Zhang, G. Liu, Y. Liang, J. Hu and B. Yi, Electrochem. Commun., 8, 707 (2006).

[70] H. Zhong, H. Zhang, Y. Liang, J. Zhang, M. Wang and X. Wang, J. Power Sources, 164, 572 (2007).

[71] J. Giner and L. Swette, *Nature*, **211**, 1291 (1966).

[72] M. Nie, P.K. Shen, M. Wu, Z. Wei and H. Meng, J. Power Sources, 162, 173 (2006).

[73] J. Yang, J.Y. Lee, Z. Zhang, W. Zhou, Z. Liu, J. Electrochem. Soc., 155, B776 (2008).

[74] J. Yang, C.H. Cheng, W. Zhou, J.Y. Lee, Z. Liu, Fuel Cells, 2010, DOI: 10.1002/fuce.200900205.

[75] A. Kelly, G.W. Groves, P. Kidd, Crystallography and Crystal Defects, Revised Edition, Wiley, New York, 2000.

[76] M. De Graef, M. E. McHenry, Structure of Materials, Cambridge University Press, New York, 2007.

[77] T. Shibata, B. A. Bunker, Z. Zhang, D. Meisel, C. F. Vardeman, J. D. Gezelter, J. Am. Chem. Soc. 124 (2002) 11989-11996.

[78] G. Ouyang, X. Tan, C.X. Wang, G.W. Yang, Chem. Phys. Lett., 420, 65 (2006).

[79] R. E. Benfield, J. Chem. Soc. Faraday Trans., 88, 1107 (1992).

[80] H. Borchert, E.V. Shevchenko, A. Robert, I. Mekis, A. Kornowski, G. Grenoble, H. Weller, Langmuir, 21, 1931 (2005).

[81] A. Sarkar, A.V. Murugan, A. Manthiram, Langmuir, 26, 2894 (2010).

[82] T.H. Yu, Y. Sha, B.P. Merinov, W.A. Goddard, J. Phys. Chem. C, 114, 11527 (2010).

[83] L. Tang, B. Han, K. Persson, C. Friesen, T. He, K. Sieradzki, G. Ceder, J. Am. Chem. Soc., 132, 596 (2010).